International Journal of Thermal Sciences 185 (2023) 108058

Contents lists available at ScienceDirect

International Journal of Thermal Sciences

journal homepage: www.elsevier.com/locate/ijts

A numerical investigation of the particle behaviors and entropy generation in mixed convection inside a vented enclosure

Oktay Çiçek [a], A. Cihat Baytaş [b,*]

[a] Faculty of Aeronautics and Astronautics, Istanbul Technical University, Maslak, 34469 Istanbul, Turkey
[b] Faculty of Engineering and Architecture, Istanbul Gelisim University, Avcılar, 34310 Istanbul, Turkey

ARTICLE INFO

Keywords:
Eulerian–Lagrangian approach
Mixed convection
Entropy generation
Particle distribution and deposition
Vented cavity

ABSTRACT

The present study is to focus on the numerical investigation of the transportation, deposition and removal of solid particles in the range of 5 μm to 0.01 μm for mixed convection flow in the vented square cavity by utilizing the Eulerian–Lagrangian method with one-way coupling. The change in the deposition and removal mechanisms affected by the forces acting on the particles is addressed for mixed convection of ventilation airflow. In the analysis of entropy generation, the irreversibilities due to the presence of solid particles are studied with a new approach for both dominant natural and forced convection. The governing equations for fluid phase and the Lagrangian particle tracking are scrutinized by employing the finite volume method with SIMPLE algorithm and explicitly integrating the set of ordinary differential equations, respectively. The examination of the thermal and flow fields is carried out in the cases of various Reynolds numbers and Richardson numbers. The minimum and maximum values of the average Nusselt number are determined with related operating parameters. By using the results of thermal behaviors and flow structures obtained at steady-state condition, the particle velocity, temperature and location are presented for the combined natural and forced convection. By investigating the particles deposited on the walls and ones removed from the exit section for different Reynolds numbers and Richardson numbers, it is demonstrated that the sum rate of deposition and removal is low at $1 \leq Ri \leq 10$ and high Reynolds number for 1 μm and 0.1 μm particles. For given Reynolds number, increasing the buoyancy effect results in substantial changes in the thermal field and flow pattern, therefore the particles remaining suspended show different behaviors when the effect of natural convection alters from weak to dominant. It is observed that the Brownian and thermophoretic forces play an important role in the small particle deposition and removal. As a result of entropy generation analysis, the minimum total entropy generation is determined at $Ri = 5$ for given Reynolds number except for $Re = 50$. Moreover, it is proposed to investigate the irreversibilities due to the heat transfer between the particles and the fluid surrounding them and the frictional total force acting on the suspended particles.

1. Introduction

The particle behavior has received the significant attention because there is a wide range of engineering and environmental applications including indoor environment, chemical reactor, energy system [1,2], ventilation system, medical field [3,4], porous media [5] and so on. It is essential to comprehend the effects of particle behaviors consisting of deposition, removal, dispersion, agglomeration, and sedimentation on these applications [6]. It is vital to diminish the infection risks in indoor spaces, such as hospitals and schools [7,8]. In addition, the transmission of contaminants and diseases in an aircraft cabin can be reduced by an effective ventilation system [9,10]. For this purpose, one of the primary measures is appropriate ventilation design, resulting in the removal of more particles from indoor environments [11]. Due to the crucial effects of mixed convection heat transfer based on the inertial and buoyancy forces in the vented cavity, it has an important role in many industrial applications, such as air conditioning, thermal energy storage systems, solar energy collectors, electronic cooling, thermal insulation systems and heat exchangers [12,13]. The examination of heat transfer enhancement can be analyzed by considering the external and buoyancy-driven flows under the various thermal boundary conditions and geometric configurations.

In the literature, there are many studies which present the results of mixed convection in the ventilated enclosure. Sourtiji et al. [14] investigated the mixed convection in a vented square cavity with the pulsating incoming flow. The findings displayed the optimal Strouhal number related to the enhancement of heat transfer and pressure drop.

* Corresponding author.
E-mail address: acbaytas@gelisim.edu.tr (A.C. Baytaş).

https://doi.org/10.1016/j.ijthermalsci.2022.108058
Received 14 May 2022; Received in revised form 29 October 2022; Accepted 22 November 2022
Available online 13 December 2022

List of Symbols

a	Height of inlet section (m)
A	Dimensionless height of inlet section, Eq. (7)
A_p	Particle surface area (m^2), Eq. (19)
c_p	Specific heat capacity ($Jkg^{-1}K^{-1}$)
C	Cunningham slip correction factor, Eq. (11)
C_T	Thermophoretic coefficient, Eq. (15)
d_p	Particle diameter (m)
f	Stokes–Cunningham drag coefficient, Eq. (11)
F_B	Brownian force (N), Eq. (13)
F_D	Drag force (N), Eq. (10)
F_G	Gravity force (N), Eq. (12)
F_L	Saffman's lift force (N), Eq. (17)
F_T	Thermophoresis force (N), Eq. (14)
F_{tot}	Total force acting on a particle (N), Eq. (24)
g	Gravitational acceleration (ms^{-2})
G	Independent Gaussian random number
Gr	Grashof number, Eq. (7)
h	Heat transfer coefficient ($Wm^{-2}K^{-1}$)
k	Thermal conductivity ($Wm^{-1}K^{-1}$)
Kn	Knudsen number, Eq. (16)
L	Side length (m), Eq. (21)
m_p	Particle mass (kg)
np	Number of suspended particles
N_{gen}	Total entropy generation, Eq. (26)
Nu	Local Nusselt number, Eq. (5)
Nu_p	Particle Nusselt number, Eq. (19)
$\overline{Nu}$	Average Nusselt number, Eq. (5)
p	Pressure (Nm^{-2})
P	Dimensionless pressure
Pr	Prandtl number, Eq. (7)
Re	Reynolds number, Eq. (7)
Re_p	Particle Reynolds number, Eq. (19)
Ri	Richardson number, Eq. (7)
$\dot{S}'''$	Entropy generation rate per unit volume ($WK^{-1}m^{-3}$), Eq. (23)
S_{gen}	Local entropy generation, Eq. (25)
t	Time (s)
T	Temperature (K)
$(T_{fp})_{ave}$	Ratio of the sum of the absolute temperature differences to the number of suspended particles (K), Eq. (20)
u, v	Velocity components along x and y axes, respectively (ms^{-1})
u_{in}	Inlet velocity (ms^{-1}), Eq. (21)
U, V	Dimensionless velocity components in X and Y direction
V_r	Relative velocity (ms^{-1})
x, y	Cartesian Coordinates (m)
X, Y	Dimensionless Coordinates
$\forall$	Volume (m^3)

Greek Symbols

α	Thermal diffusivity (m^2s^{-1})
β	Thermal expansion coefficient (K^{-1})
Θ	Dimensionless temperature, Eq. (7)
κ	Boltzmann constant (JK^{-1})
λ	Mean free path (m)
μ	Dynamic viscosity ($kgm^{-1}s^{-1}$)
ν	Kinematic viscosity (m^2s^{-1})
ρ	Density (kgm^{-3})
τ	Dimensionless time, Eq. (7)
χ	Irreversibility distribution ratio, Eq. (7)
Ψ	Non-dimensional stream function, Eq. (7)
ψ	Stream function (m^2s^{-1})

Subscripts

c	Cold
f	Fluid
h	Hot
i	Direction indicators
in	Inlet
p	Particle

Chamkha et al. [15] numerically studied the convective heat transfer in an air-filled square cavity involving a square cylinder. They showed the significant role of the inner square cylinder in the flow structure and thermal field. Selimefendigil and Öztop [16] conducted a study of mixed convection of pulsating flow in a ventilated enclosure with multiple ports, considering the effects of Reynolds number, Grashof number and Strouhal number on the heat transfer process. It was observed that the Grashof number plays a critical role in the heat transfer enhancement for higher Strouhal numbers. Gupta et al. [17] numerically solved the problem of mixed convective heat transfer in a ventilating cavity with a circular cylinder. Their outcomes reported that the cylinder size affects the temperature distributions and flow characteristics. The study on mixed convection by Biswas et al. [18] was carried out in the grooved channel with injection. The results elucidated that the use of injection improves the heat transfer rate. Yang and Wu [19] conducted the problem of conjugate mixed convection flow in the entrance region of a vertical channel by evaluating the assisted buoyancy for thermal and flow characteristics. They investigated the impacts of the wall thermal conduction on the thermal field and flow structure and the critical buoyancy parameter for some operating parameters. Nosonov and Sheremet [20] introduced the results of conjugate mixed convection in a channel with a cavity in the presence of a local heater. The investigation of mixed convection in a vented cavity with ports was done by Ismael and Jasim [21], by taking into account the fluid–structure interaction. It was observed that the presence of a flexible elastic fin located at the bottom wall improves the heat transfer mechanism. The problem of mixed convection in a channel with two facing cavities was addressed by García et al. [22] to demonstrate the influences of important parameters such as cavity aspect ratio and inclination angle. The results showed the importance of the cavity aspect ratio related to the behaviors of the system. In the study by Nasseri et al. [23], the mixed convection in a square cavity with a ventilation jet generated by a fan was scrutinized by performing the lattice Boltzmann method. The findings presented the convenient fan location, Reynolds number and Rayleigh number in terms of heat transfer enhancement. Younsi et al. [24] surveyed the effects of outlet location on thermal comfort and indoor air quality for convective heat transfer in the vented cavity containing an air–CO_2 mixture. They determined the proper ventilated configuration to enable better ventilation efficiency and indoor air quality. Ezzaraa et al. [25] scrutinized the thermal radiation and mixed convection in a ventilating enclosure with multiple ports. The obtained results clarified that enhancing the convective heat transfer is strongly dependent on

the emissivity of the walls, Reynolds number and the location of the exit port. The experimental study on mixed convective heat transfer with surface radiation was performed by Rajamohan et al. [26]. They indicated the influences of Reynolds number and surface emissivity on the heat transfer mechanism. Dhahad et al. [27] probed the problem of mixed convective heat transfer in a vented square cavity with cold incoming airflow in terms of the effective cooling performance. They determined the convenient port size and location to achieve a better efficient cooling system for the given Richardson number and Reynolds number. The review paper by Lukose and Basak [28] evaluated the numerical and experimental studies on mixed convection in terms of the different thermal and kinematic boundary conditions for various models. A numerical investigation was carried out by Velkennedy et al. [29] to assess the mixed convection in terms of thermal behavior and flow structure considering the effects of cold portions involved in the vented cavity. They proposed a correlation equation between the mean Nusselt number and Rayleigh number. Recent work by Prakash and Singh [30] numerically and experimentally analyzed the problem of mixed convection with surface radiation in a vented enclosure. The impacts of Richardson number, Reynolds number, aspect ratio, and emissivity on cooling performance were presented. Mebarek-Oudina et al. [31] focused on the convective heat transfer in a channel involving an open trapezoidal cavity to investigate the thermal and flow behaviors, taking into consideration the lid-driven walls and the discrete heat sources. The authors revealed that an increase in Reynolds number and Richardson number causes the average Nusselt number to rise.

Several published papers related to particle motion are available in the literature, using one-way coupled Eulerian–Lagrangian approach. Akbar et al. [32] worked on the particle migration in natural convection. The results presented the importance of thermophoretic and Brownian forces in small particles. Bagheri et al. [33] dealt with the particle deposition and transport in the square cavity. It was found that the change in Rayleigh number distinctly affects the flow characteristics and particle behavior. Ding et al. [34] numerically simulated the deposition and distribution of solid particles in a ventilating cavity by using the Lagrangian particle tracking and the lattice Boltzmann methods. Golkarfard et al. [35] reported numerical results of the particle deposition in mixed convection. The results introduced the decrease in deposition rate with a rising Richardson number. Golkarfard and Talebizadeh [36] presented the numerical simulation of particle deposition and dispersion in the cases of radiator and floor heating systems. The findings indicated that the floor heating system further increases the deposition of particles compared to the radiator heating one. The numerical investigation of Garoosi et al. [37] on particle transport and deposition was considered for natural convection in an enclosure with heaters and coolers. By applying one-way coupling method, the outcomes showed that the effect of thermophoresis force on 1 μm particles is stronger. The numerical study on particle migration and deposition in the regular and irregular structure filters was performed by Ansari et al. [38], using the lattice Boltzmann method for laminar flow. The findings indicated the rate of particle deposition on the first block gets the highest value. Inthavong et al. [39] considered the numerical problem of particle dispersion and deposition in confined flow, using the Euler Implicit scheme. Mahdavi et al. [40] presented the numerical study on mixed convection of tube flow at different inclination angles to evaluate the influences of nanoparticles on the thermal and flow fields. It was demonstrated that the Van der Waals adhesion force has a very significant effect on particle deposition, whereas the gravitational effect has a slight role in particle behavior. Yin et al. [41] numerically and experimentally analyzed the convective heat transfer of nanofluid in a tube by employing discrete phase model. Their results displayed that a decrease in the particle diameter and an increment in particle volume fraction lead to higher particle deposition rate. The work of Han et al. [42] focused on the ash particle deposition process in a three-dimensional rectangular heat transfer channels, and it was clarified that the particle behavior is significantly affected by the particle size and flow velocity. Talebizadehsardari et al. [43] used one-way coupled Eulerian–Lagrangian approach to investigate the small particle distribution and deposition in an annular pipe, and the authors proposed a new correlation equation of particle deposition as a function of the dimensionless diffusion parameter. The nanoparticles motion and forced convection in a wavy-wall channel were numerically studied by Alsabery et al. [44]. The findings of this paper found that the average particle velocity becomes higher with increasing Reynolds number and number of oscillations. Lu and Quan [45] presented the numerical study of particle deposition in a three-dimensional ribbed heat exchange channel for turbulent flow. Jahanbin and Semprini [46] conducted the problem of indoor particle behavior in the heat recovery ventilation, considering the effects of ventilation and heat source, and as a result of this work, it was demonstrated that an increment in the ventilation rate causes the heating system to have a weaker effect on the particle decay.

The entropy generation related to the efficiency and thermal performance of the thermodynamics system is an important topic in the convective processes. An inherent irreversible process observed for all engineering applications causes some available work of the system to be destroyed. Therefore, the minimization of entropy generation due to heat transfer and fluid friction has a significant effect on the increase in the efficiency of the system and the reduction in the destroyed work [47]. From this point of view, by employing the second law of thermodynamics, Entropy Generation Minimization (EGM) has a crucial role in the thermal design and optimization of the systems [48]. Narusawa [49] numerically and theoretically investigated the entropy generation analysis and mixed convection in a rectangular duct. Chen et al. [50] studied the entropy generation for mixed convective heat transfer in a vertical channel by taking into account the viscous dissipation, and their results showed that the lower entropy generation rate and higher Bejan number are observed in the vicinity of the centerline. The numerical investigation of entropy generation in a three-dimensional rectangular duct for buoyancy opposed mixed convection was conducted by Yang and Wu [51]. They introduced the effects of opposed buoyancy force on entropy generation due to heat transfer and viscous dissipation. Hussein [52] numerically analyzed the second law of thermodynamics within mixed convection in a three-dimensional triangular cavity with moving the vertical wall. The findings presented the variation of entropy generation in terms of Richardson number and the direction of the moving wall. For mixed convective heat transfer in an oblique vented cavity with inlet and outlet port, the entropy generation analysis was carried out by Gupta and Nayak [53], and the effects of inclination angle, Richardson number and Reynolds number on irreversibility in the system were discussed. Çiçek and Baytaş [54] scrutinized the entropy generation of conjugate forced convection flow in a semi-cylindrical vented cavity with one inlet and two outlet ports. In this paper, the total entropy generation number and average Bejan number were obtained for different Reynolds numbers under various geometric configurations. The study of Çiçek and Baytaş [55] reported the results of entropy generation for conjugate forced convection with porous media in a cylindrical vented cavity. They presented the minimum total entropy generation number for various Reynolds numbers and thermal conductivity ratios. Hamzah et al. [56] numerically solved the problem of entropy generation for mixed convection in a ventilated cavity involving rotating cylinders. It was observed that the rotating cylinders strongly affect the entropy generation. Selimefendigil and Öztop [57] focused on the entropy generation of mixed convection nanofluid flow in a vented cavity in the presence of a magnetic field. They revealed that increasing the Hartmann number causes the total entropy generation to first decrease, and then increase. The numerical investigation of mixed convection and entropy generation for hybrid nanofluid flow was performed by Benzema et al. [58], and the outcomes showed the impacts of Hartmann number, Reynolds number and nanoparticle volume fraction on Bejan

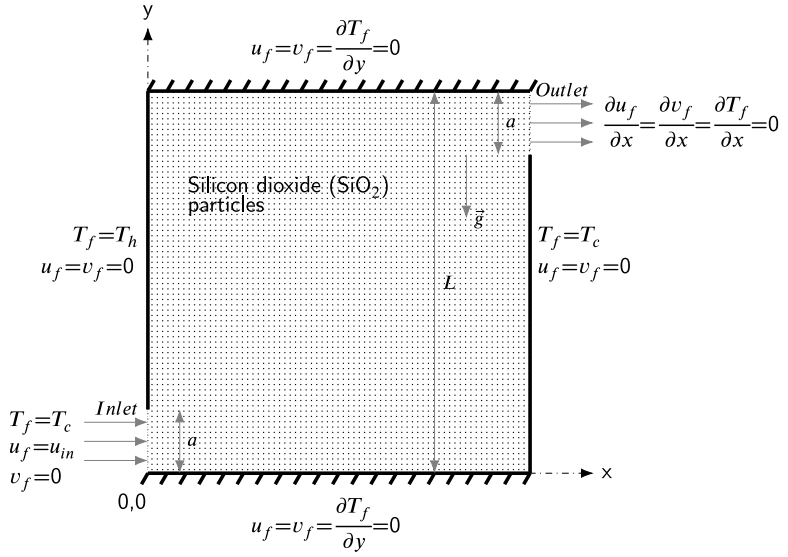

Fig. 1. A schematic representation of the vented square cavity.

Table 1
Thermophysical characteristics of SiO_2 and air at 323 K.

	ρ (kg/m^3)	k (W/mK)	c_p (J/kgK)	μ (mPa s)	β (K^{-1})
SiO_2	2220.0	1.38	745.0	–	–
Air	1.085	0.028	1007.0	0.01964	3.12×10^{-3}

number and total entropy generation in a vented trapezoidal enclosure. The study of entropy generation of mixed convection for nanofluid flow in a porous annulus with a rotating cylinder by Çiçek et al. [59] presented the minimum total entropy generation numbers related to the key parameters.

The main aim of the present work is to study the particle transport and mixed convection in the ventilating enclosure using the one-way coupled Eulerian–Lagrangian method. The change in particle behavior is studied concerning the forces acting on solid particles in various thermal and flow fields. Numerical analysis of the entropy generation in combined free and forced convection is performed by taking into account the irreversibilities owing to the presence of particles. The thermal fields and flow structures of airflow are analyzed in the cases of different Reynolds numbers and Richardson numbers in the ranges of 50–500 and 0.1–20, respectively. The variation of the average Nusselt numbers on the hot wall is presented with the effect of the incoming fluid flow. The influences of mixed convection on the behaviors of particles are investigated with regard to heat transfer mechanism and flow pattern. It is presented that the forces acting on the particles have a significant role in the particle deposition on the walls and removal from the outlet port. The variations of suspended particle rates versus Richardson number are given at the various Reynolds numbers and particle sizes. For given parameters, the distributions of particle velocity and temperature are studied, while the local thermal equilibrium between the particle and the fluid surrounding it is examined in terms of the particle size. By applying the second law of thermodynamics, the entropy generation analysis is also performed for the presence of the suspended particles in the host fluid by considering the irreversibility due to thermal gradients and fluid friction. The entropy generation due to heat transfer between particles and fluid and frictional total force is investigated in detail for different Reynolds numbers, Richardson numbers and particle diameters.

2. Physical and mathematical statement of the problem

The problem of mixed convection and entropy generation in a square vented enclosure is scrutinized, taking into account the behaviors of particles. As depicted in Fig. 1, the left wall has a constant high temperature T_h (373 K), while the right wall and incoming fluid with u_{in} velocity have a fixed low temperature T_c (273 K). The length of the cavity side and the height of the inlet and outlet sections are L and $a = 0.1L$, respectively. Thermophysical characteristics of SiO_2 particles and air are demonstrated in Table 1. The one-way coupled Eulerian–Lagrangian approach is performed to investigate the transport and deposition of particles, as well as the solid particle removed from the outlet port. The influences of solid particles on the thermal and flow behaviors can be neglected since the volume fraction of particles in the host fluid is very low.

The flow is assumed to be incompressible, Newtonian, laminar, and two-dimensional with the Boussinesq approximation are considered. The non-dimensional governing equations for the fluid phase are as follows:

The non-dimensional continuity equation is:

$$\frac{\partial U_f}{\partial X}+\frac{\partial V_f}{\partial Y}=0 \tag{1}$$

The non-dimensional momentum balance equation in the X-direction is given as:

$$\frac{\partial U_f}{\partial \tau}+U_f\frac{\partial U_f}{\partial X}+V_f\frac{\partial U_f}{\partial Y}=-\frac{\partial P}{\partial X}+\frac{2a}{L}\frac{1}{Re}\left[\frac{\partial^2 U_f}{\partial X^2}+\frac{\partial^2 U_f}{\partial Y^2}\right] \tag{2}$$

The non-dimensional momentum balance equation in the Y-direction is:

$$\frac{\partial V_f}{\partial \tau}+U_f\frac{\partial V_f}{\partial X}+V_f\frac{\partial V_f}{\partial Y}=-\frac{\partial P}{\partial Y}+\frac{2a}{L}\frac{1}{Re}\left[\frac{\partial^2 V_f}{\partial X^2}+\frac{\partial^2 V_f}{\partial Y^2}\right]+\left(\frac{2a}{L}\right)^2\frac{Gr}{Re^2}\Theta_f \tag{3}$$

The non-dimensional energy balance equation is as follows:

$$\frac{\partial \Theta_f}{\partial \tau}+U_f\frac{\partial \Theta_f}{\partial X}+V_f\frac{\partial \Theta_f}{\partial Y}=\frac{2a}{L}\frac{1}{RePr}\left[\frac{\partial^2 \Theta_f}{\partial X^2}+\frac{\partial^2 \Theta_f}{\partial Y^2}\right] \tag{4}$$

The local and average Nusselt numbers on the vertical hot wall are defined as:

$$Nu_f=-\frac{L-a}{L}\left(\frac{\partial \Theta_f}{\partial X}\right)_{wall}, \qquad \overline{Nu}_f=-\int_A^1\left(\frac{\partial \Theta_f}{\partial X}\right)_{wall}dY \tag{5}$$

The non-dimensional initial and boundary conditions are expressed as:

$$\tau = 0; \quad U_f = V_f = \Theta_f = P = 0 \quad \text{everywhere}$$
$$\tau > 0;$$
$$\text{at inlet section } (0 \le Y < A,\ X = 0); \quad U_f = 1, \quad T_f = V_f = 0, \quad \Psi = Y$$
$$\text{at outlet section } (1 - A < Y \le 1,\ X = 1);$$
$$\frac{\partial U_f}{\partial X} = \frac{\partial V_f}{\partial X} = \frac{\partial \Theta_f}{\partial X} = \frac{\partial^2 \Psi}{\partial X^2} = 0$$
$$\text{at vertical left wall } (A \le Y \le 1,\ X = 0); \quad \Theta_f = 1,$$
$$U_f = V_f, \quad \Psi = A = 0$$
$$\text{at vertical right wall } (0 \le Y \le 1 - A,\ X = 1); \quad \Theta_f = U_f = V_f = \Psi = 0$$
$$\text{at top wall } (0 \le X \le 1,\ Y = 1); \quad \frac{\partial \Theta_f}{\partial Y} = U_f = V_f = 0, \quad \Psi = A$$
$$\text{at bottom wall } (0 \le X \le 1,\ Y = 0); \quad \frac{\partial \Theta_f}{\partial Y} = U_f = V_f = \Psi = 0 \tag{6}$$

The non-dimensional variables used to obtain the above non-dimensional governing equations are defined as follows:

$$X = \frac{x}{L}, \quad Y = \frac{y}{L}, \quad U_f = \frac{u_f}{u_{in}}, \quad V_f = \frac{v_f}{u_{in}}, \quad \tau = \frac{t u_{in}}{L}, \quad \Theta_f = \frac{T_f - T_c}{T_h - T_c},$$
$$P = \frac{p}{\rho_f u_{in}^2}, \quad \Psi = \frac{\psi}{u_{in} L}, \quad Gr = \frac{g \beta_f \Delta T L^3}{\nu_f^2}, \quad Re = \frac{u_{in} 2a}{\nu_f}, \quad Pr = \frac{\nu_f}{\alpha_f},$$
$$Ri = \frac{Gr}{Re^2},$$
$$\Delta T = T_h - T_c, \quad A = \frac{a}{L}, \quad S_{gen} = \dot{S}''' \frac{T_0^2 L^2}{k_f (\Delta T)^2}, \quad \chi = \frac{\mu_f T_0}{k_f} \left(\frac{u_{in}}{\Delta T} \right),$$
$$T_0 = \frac{T_h + T_c}{2} \tag{7}$$

The Lagrangian method enables the trajectories of the particles in the host fluid to be tracked individually. The location and motion of the particles are changed by the forces acting on them, and these forces are subject to the effect of fluid flow. The influences of particles on the fluid flow and the interactions between particles can be neglected by the reason of the low particle volume fraction (lower than 10^{-6}). Therefore, the one-way coupling approach is applied in the analysis of particle behaviors related to the location, velocity, temperature, deposition and dispersion. These properties are recalculated and updated at each particle time step during tracking the solid particle [6]. The rotational motion of particles is ignored in this study. After calculating the flow and temperature fields at steady-state condition, the behaviors of particles are examined in the Lagrangian frame using the one-way coupled Eulerian–Lagrangian method. Newton's law of motion is applied to determine the particle velocity and location. The equations of particle motion in the Lagrangian reference frame can be given as [60]:

$$\rho_p V_p \frac{du_{p,i}}{dt} = F_{D,i} + F_{G,i} + F_{B,i} + F_{T,i} + F_{L,i} \tag{8}$$

$$\frac{dx_i}{dt} = u_{p,i} \tag{9}$$

where $i = 1$ and 2 express x and y directions. The left-hand side of Eq. (8) is related to the particle inertia, while in the right hand side of Eq. (8), the first term is the drag force, the second term is the gravity force, the third term defines the Brownian force, the fourth term represents the thermophoresis effect and the last term is Saffman's lift force. There should be equality between the inertial force and the forces acting on a particle.

By employing the Stokes' law, the hydrodynamic drag force on the particles is defined by:

$$F_{D,i} = f \left(u_{f,i} - u_{p,i} \right) \tag{10}$$

$f = \frac{3\pi \mu_f d_p}{C}$ is Stokes–Cunningham drag coefficient,

$$C = 1 + \frac{2\lambda}{d_p} \left[a_1 + a_2 \exp\left(-a_3 \frac{d_p}{2\lambda} \right) \right], \tag{11}$$
$$a_1 = 1.252, a_2 = 0.399, a_3 = 1.10$$

The gravitational force is given as:

$$F_{G,i} = \left(\rho_p - \rho_f \right) V_p g_i \tag{12}$$

The random motion of particles can be analyzed by the Brownian force resulting from the kinetic energy and temperature of the particles in the host fluid. This force can be expressed by [60]:

$$F_{B,i} = G_i \sqrt{\frac{6\pi \mu_f d_p \kappa T_f}{C \Delta t}} \tag{13}$$

where Δt is the time step in Lagrangian frame, G_i is the Gaussian random number with zero mean and unit variance, and $G_x = \sqrt{-2 \ln U_1} cos(2\pi U_2)$ and $G_y = \sqrt{-2 \ln U_2} cos(2\pi U_1)$ and U_1 and U_2 get random values between zero and one.

The thermophoresis force arising from the high temperature gradient leads to push the particles to the cold zone. The following equation defines this force [61]:

$$F_{T,i} = -f \frac{C_T \nu_f}{T_f} \nabla_i T \tag{14}$$

where

$$C_T = \frac{2.34 \left(k_f / k_p + 2.18 Kn_p \right) C}{\left(1 + 3.42 Kn_p \right) \left(1 + 2k_f / k_p + 4.36 Kn_p \right)} \tag{15}$$

$$Kn_p = 2 \frac{\lambda}{d_p} \tag{16}$$

The effect of the shear field depending on the inertia effect of viscous flow on the particles can be examined by the Saffman's lift force given as [62]:

$$F_{L,x} = 1.615 \rho_f \nu_f^{0.5} d_p^2 \left(u_f - u_p \right) \sqrt{\left| \frac{dv_f}{dx} \right|} \operatorname{sign} \left(\frac{dv_f}{dx} \right)$$
$$F_{L,y} = 1.615 \rho_f \nu_f^{0.5} d_p^2 \left(v_f - v_p \right) \sqrt{\left| \frac{du_f}{dy} \right|} \operatorname{sign} \left(\frac{du_f}{dy} \right) \tag{17}$$

By using the first law of thermodynamics, the energy balance equation for particles can be defined as follows [63]:

$$m_p (c_p)_p \frac{dT_p}{dt} = h A_p \left(T_f - T_p \right) \tag{18}$$

where A_p is the particle surface area, h is the heat transfer coefficient proposed by Ranz and Marshall [64]. The convective heat transfer between the fluid phase and the particle is scrutinized in the Lagrangian frame without considering the radiation heat transfer and internal particle heat transfer resistance. Due to very low Biot number for the particle, the uniform temperature distribution within the particle is assumed.

$$Nu_p = \frac{h d_p}{k_f} = 2 + 0.6 Re_p^{1/2} Pr^{1/3}$$
$$Re_p = \frac{d_p}{\nu_f} \sqrt{\left(u_p - u_f \right)^2 + \left(v_p - v_f \right)^2} \tag{19}$$
$$A_p = \pi d_p^2$$

where Re_p represents the particle Reynolds number depending on the particle size and the relative velocity.

An investigation of the local thermal equilibrium between small solid particles and the fluid surrounding those can be carried out by the following equation, representing the ratio of the sum of the absolute temperature differences to the number of suspended particles (np). It

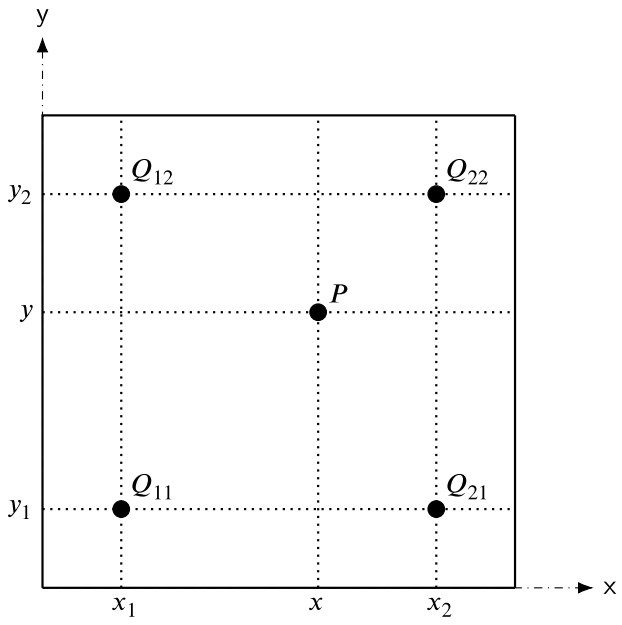

Fig. 2. The schematic of bilinear interpolation for Lagrangian particle tracking.

can be emphasized that as the value of $(T_{fp})_{ave}$ approaches zero, the local thermal equilibrium is achieved.

$$(T_{fp})_{ave} = \frac{1}{np}\sum_{np}|T_f - T_p| \tag{20}$$

First, the cavity size (L) is computed for given Grashof number with $\Delta T = 100$ K, and then the inlet velocity (u_{in}) is determined from Reynolds number for the dimensional analysis of Lagrangian particle tracking, as indicated below:

$$L = \left(\frac{Gr \cdot \nu_f^2}{g\beta_f \Delta T}\right)^{(1/3)}, \quad u_{in} = \frac{Re \cdot \nu_f}{2a} \tag{21}$$

Minimizing entropy generation related to the heat transfer and flow structure is of great importance in terms of thermal design and optimization [69]. In the entropy generation analysis, the irreversibilities caused by thermal gradients and fluid friction are considered within the entire system, while the entropy generation that occurs due to the presence of suspended particles in the host fluid should be examined. The study of Bejan [70] includes the following entropy generation equation related to the external flow over a solid body remaining suspended in the fluid flow.

$$\dot{S}_{gen} = \left(\frac{T_w - T_\infty}{T_\infty}\right)^2 \bar{h}A + \frac{1}{T_\infty}F_D U_\infty \tag{22}$$

where T_w, F_D, h, A, T_∞ and U_∞ represent the solid body temperature, the drag force, the average convective heat transfer, solid surface area, free-stream fluid temperature and velocity, respectively. In the right of Eq. (22), the first and second terms define the entropy generation due to heat transfer across the non-zero temperature difference $T_w - T_\infty$ and drag friction. From this point of view, it is proposed to apply Eq. (22) for all suspended particles. The entropy generation can be calculated both in each particle and in a cell volume holding suspended particles. For this purpose, it is recommended to use the following local entropy generation equation after the steady-state flow condition is obtained,

Table 2
Comparison of the results for the number of particles in the range of 2000 to 20000; $Re = 300$, $Ri = 1.0$, $d_p = 1$ μm.

The number of particles	PDRF	$(F_D)_{ave}$	$(F_B)_{ave}$	$(F_T)_{ave}$	$(\bar{u}_p)_{ave}$	$(T_p)_{ave}$
2000	0.2605	294.1	389.5	19.02	0.2804	300.4
4000	0.2610	297.9	391.7	19.1	0.280	300.2
6000	0.2608	294.1	388.9	19.05	0.2803	300.8
10000	0.2577	296.3	387.0	19.04	0.2816	300.2
20000	0.2580	295.7	388.2	19.01	0.2802	300.5

and the particle trajectory is completed.

$$\begin{aligned}\dot{S}''' = {} & \frac{k_f}{T_0^2}\left[\left(\frac{\partial T_f}{\partial x}\right)^2 + \left(\frac{\partial T_f}{\partial y}\right)^2\right] \\ & + \frac{\mu_f}{T_0}\left[2\left(\left(\frac{\partial u_f}{\partial x}\right)^2 + \left(\frac{\partial v_f}{\partial y}\right)^2\right) + \left(\frac{\partial u_f}{\partial y} + \frac{\partial v_f}{\partial x}\right)^2\right] \\ & + \sum_{n_p}\frac{1}{\delta \forbar{V}}\left(\frac{(T_p - T_f)^2}{T_0^2}hA_p\right) + \sum_{n_p}\frac{1}{\delta \forbar{V}}\left(\frac{1}{T_0}F_{tot}V_r\right)\end{aligned} \tag{23}$$

$$\begin{aligned} V_r &= \sqrt{(u_p - u_f)^2 + (v_p - v_f)^2} \\ F_x &= F_{D,x} + F_{G,x} + F_{B,x} + F_{T,x} + F_{L,x} \\ F_y &= F_{D,y} + F_{G,y} + F_{B,y} + F_{T,y} + F_{L,y} \\ F_{tot} &= \sqrt{F_x^2 + F_y^2} \end{aligned} \tag{24}$$

where $\delta \forbar{V}$, np h, A_p, F_{tot} and V_r define a cell volume, the number of suspended particles inside a cell volume, convective heat transfer, particle surface area, total force acting on a particle and relative velocity, respectively. In the right hand side of Eq. (23), the first and second terms represent the heat transfer irreversibility due to the temperature gradients and fluid friction irreversibility, respectively, the third term denotes the entropy generation due to the heat transfer between the solid particles and the fluid surrounding it, and the last term defines the entropy generation due to frictional force.

In the non-dimensional form, the local entropy generation equation can be expressed as follows: see Eq. (25) that is given in Box I. where HTI and FFI identify the non-dimensional local entropy generation due to heat transfer and fluid friction. $PHTI$ and $PFFI$ are the non-dimensional local entropy generation due to particle heat transfer irreversibility and particle frictional total force irreversibility.

The total entropy generation in dimensionless form is given by integrating the non-dimensional local entropy generation over the entire vented cavity volume:

$$\begin{aligned} N_{gen} &= \int S_{gen}\, dXdY \\ &= \underbrace{\int HTI + FFI\, dXdY}_{N_{gen,f}} + \underbrace{\int PHTI\, dXdY}_{N_{PHTI}} + \underbrace{\int PFFI\, dXdY}_{N_{PFFI}} \\ &\qquad \underbrace{\qquad\qquad\qquad\qquad}_{N_{gen,p}} \end{aligned} \tag{26}$$

where $N_{gen,f}$ consists of the dimensionless total entropy generations due to heat transfer and viscous dissipation while $N_{gen,p}$ is the non-dimensional total entropy generations in the solid particles due to heat transfer between the fluid and the particles (N_{PHTI}) and frictional total force (N_{PFFI}).

3. Solution procedure

The governing differential equations (Eqs. (1) to (4)) associated with the boundary conditions discretized by the finite volume method

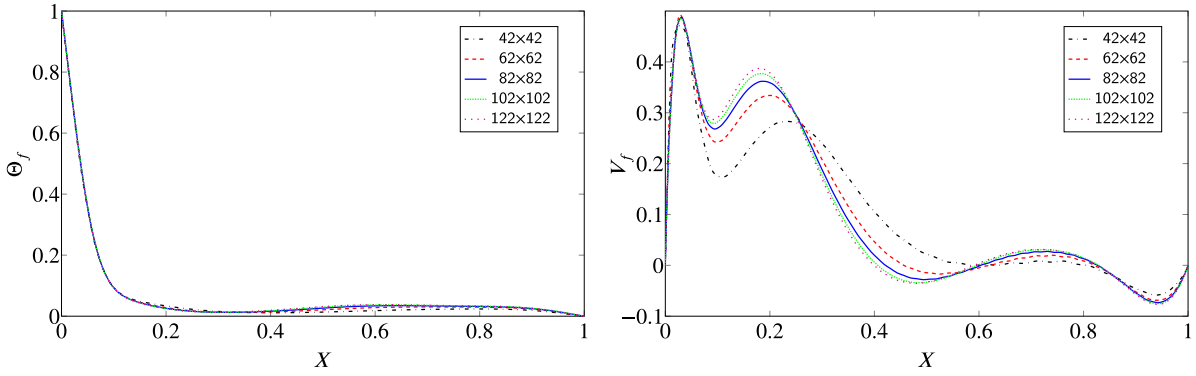

Fig. 3. The variations of the non-dimensional temperature (left) and vertical velocity (right) at middle height for different mesh sizes with $Re = 100$, $Gr = 10^6$.

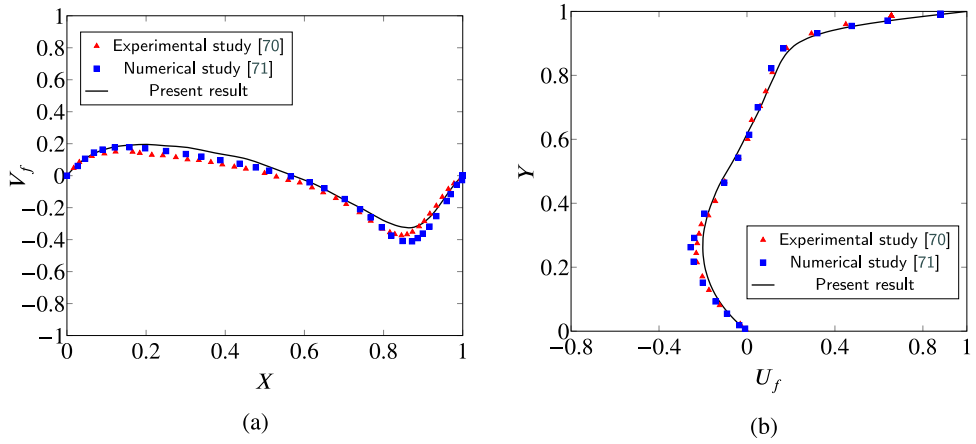

Fig. 4. The vertical (a) and horizontal (b) velocity components through the horizontal and vertical centerlines, respectively, for the lid-driven flow at $Re = 400$ compared to the experimental [65] and numerical [66] works..

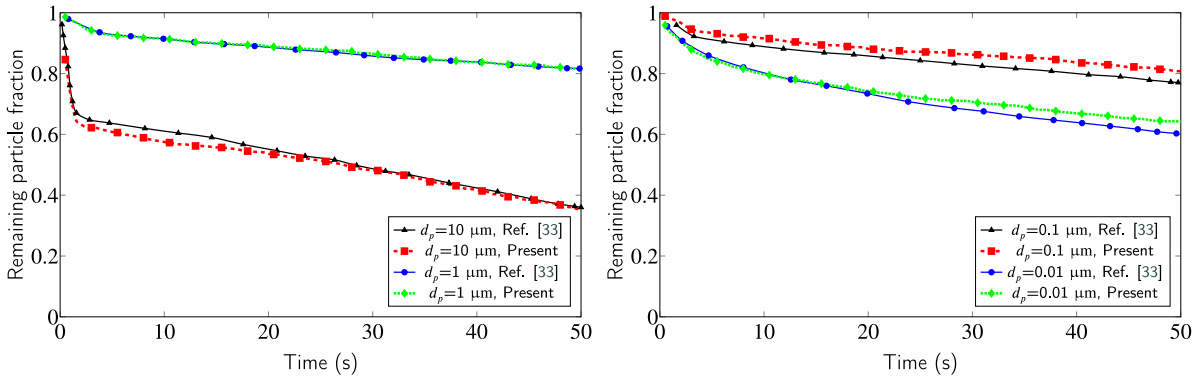

Fig. 5. The variations of suspended particle fraction for different particle diameters with $Ra = 10^5$ in comparison with the results of Bagheri et al. [33].

Table 3
Grid dependency test with $Re = 100$, $Gr = 10^6$.

Grid	42 × 42	62 × 62	82 × 82	102 × 102	122 × 122
$\overline{Nu_f}$	12.6660	11.9254	11.7327	11.6675	11.6577

with a collocated grid arrangement are solved using the SIMPLE algorithm [71], while the power-law scheme is applied for the convection and diffusion terms. To solve the system of algebraic equations, the Alternate Direction Implicit method and tri-diagonal matrix algorithm are utilized. The convergence criterion is set to 10^{-6} for the steady-state condition. The motion of particle equations (8), (9) and particle energy equation (18) are solved to demonstrate the particle distribution with their velocity and temperature by applying the Lagrange approach after satisfying the converged criterion. Table 2 demonstrates the results of suspended particles including the sum of Particle Deposition and Removal Fraction (PDRF), average drag, Brownian and thermophoresis forces (N/kg), average particle velocity (m/s) and temperature (K) for the number of particles in the range of 2000 to 20,000. The critical changes are not observed in the comparison of these results. Therefore, the number of solid particles with diameters in the range of 5 μm to 0.01 μm is set to 2000. The particles are initially located randomly with zero velocities and 273 K in the vented cavity, and the Lagrangian particle trajectory analysis is carried out over 2 s with $\Delta t = 10^{-5}$ s. The particle deposits on the walls with which it comes into contact. The particle velocity, temperature and location are calculated at each time

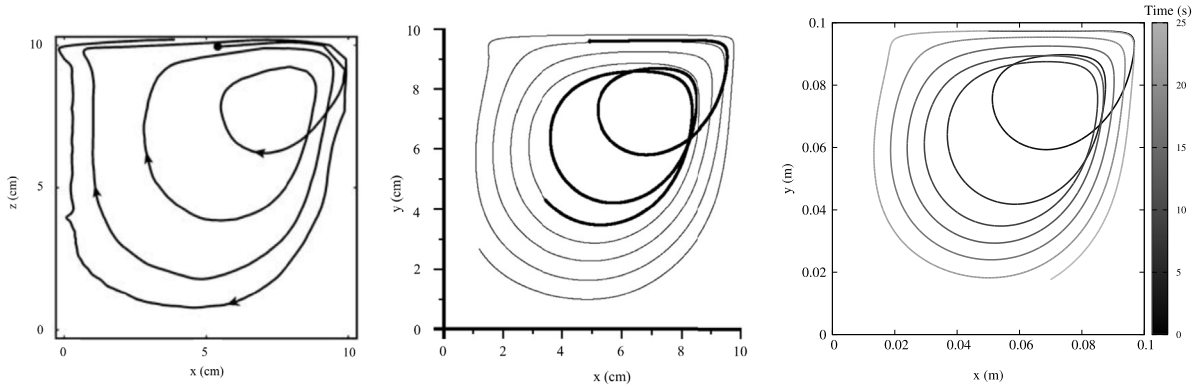

Fig. 6. Comparison of the present result (right) with the experimental work (left) [67] and the numerical study (middle) [68] for trajectory of one suspended particle with $d_p = 3$ mm inside the lid-driven cavity flow in the case of $Re = 470$.

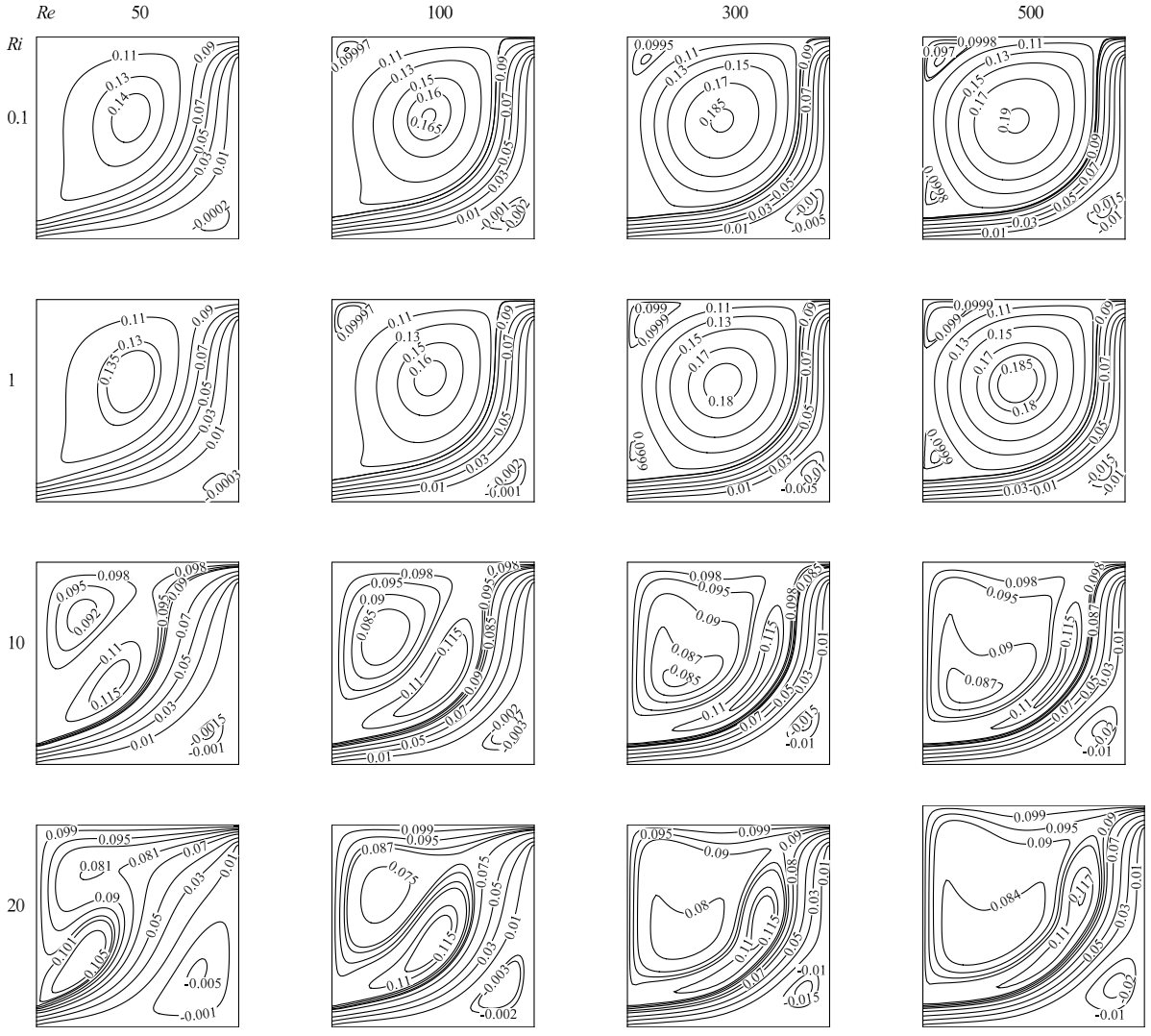

Fig. 7. Streamlines for different Reynolds numbers and Richardson numbers.

step by solving a set of ordinary differential equations (8), (9) and (18) explicitly integrated as follow [32,72]:

$$u_{p,i}^{(t+\Delta t)} = \left(u_{f,i} + \frac{B_i}{C_i}\right)^{(t)} + \left(u_{p,i} - u_{f,i} - \frac{B_i}{C_i}\right)^{(t)} \exp\left(-\frac{C_i}{A_i}\Delta t\right) \tag{27}$$

$$x_{p,i}^{(t+\Delta t)} = x_{p,i}^{(t)} + \left(u_{f,i} + \frac{B_i}{C_i}\right)^{(t)} \Delta t + \frac{A_i}{C_i}\left(u_{p,i} - u_{f,i} - \frac{B_i}{C_i}\right)^{(t)} \left[1 - \exp\left(-\frac{C_i}{A_i}\Delta t\right)\right] \tag{28}$$

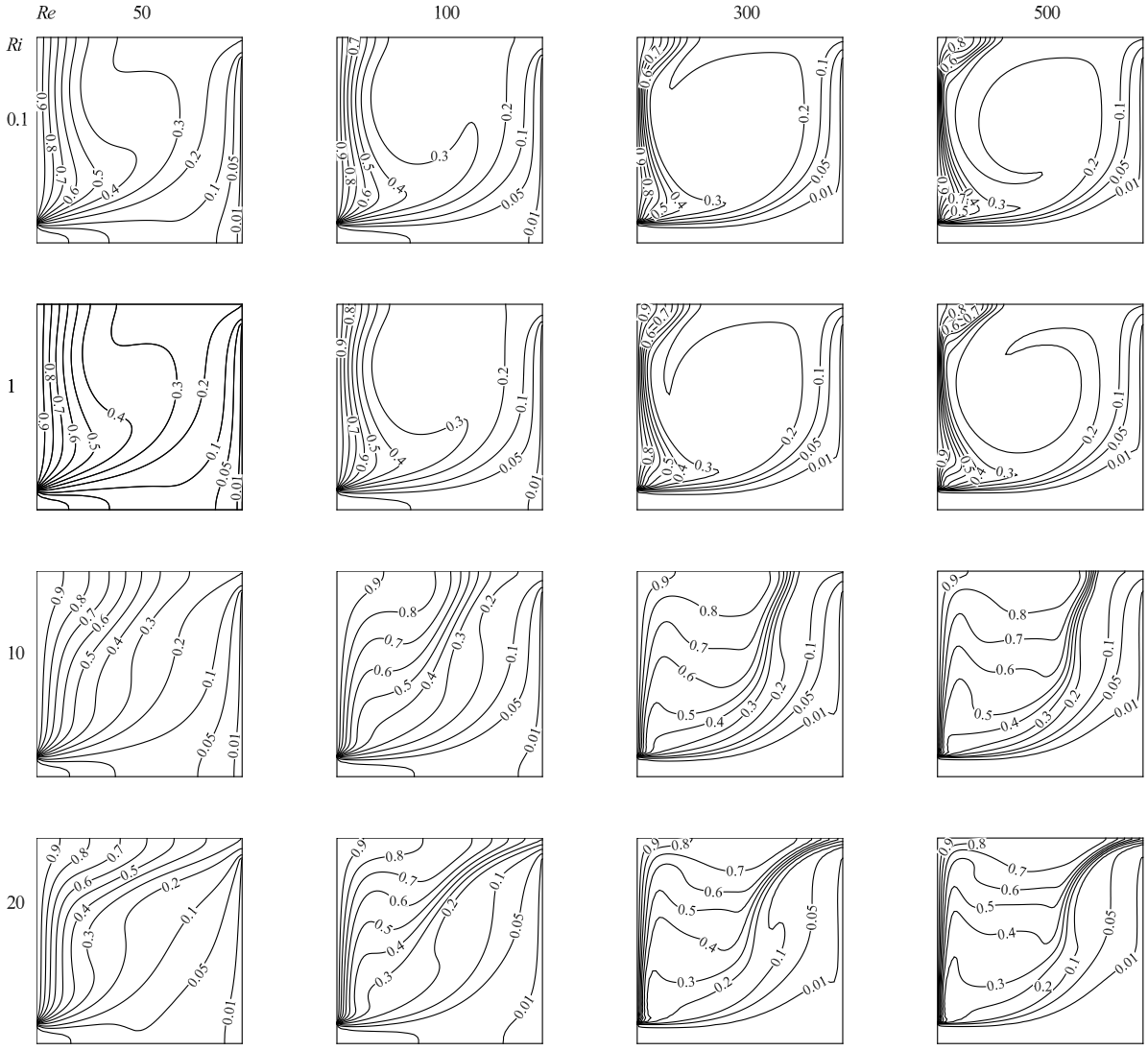

Fig. 8. Isotherms in the cases of various Reynolds numbers and Richardson numbers.

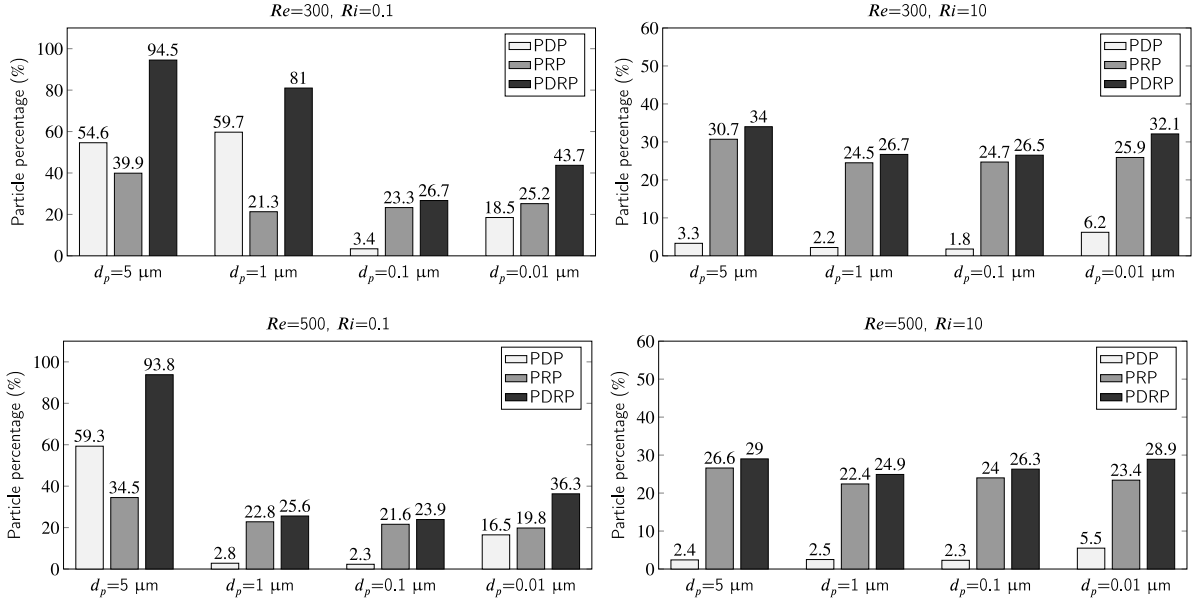

Fig. 9. Particle deposition percentage (PDP), particle removal percentage (PRP) and sum of both percentages (PDRP) for different particle diameters at $Re = 300, 500$ and $Ri = 0.1, 10$.

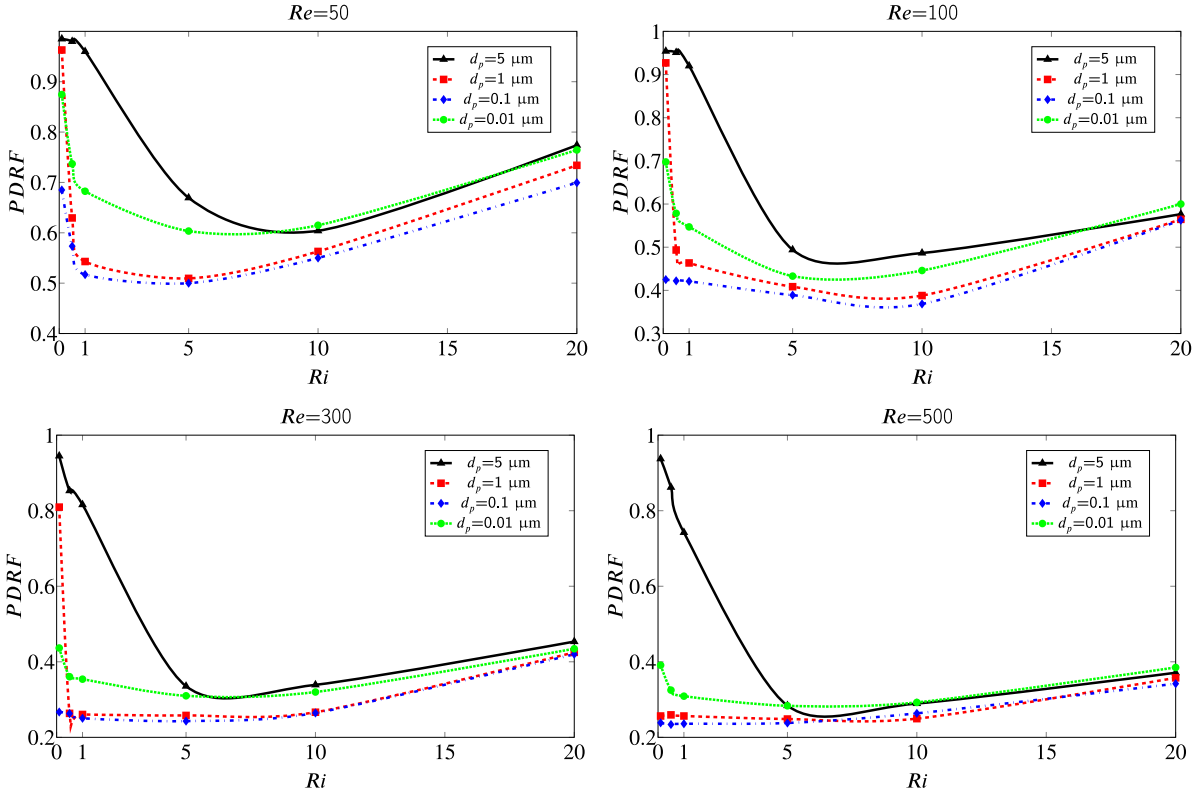

Fig. 10. The variation of the sum of the deposition and removal of particles fractions (PDRF) versus Richardson number for different Reynolds numbers and particle diameters.

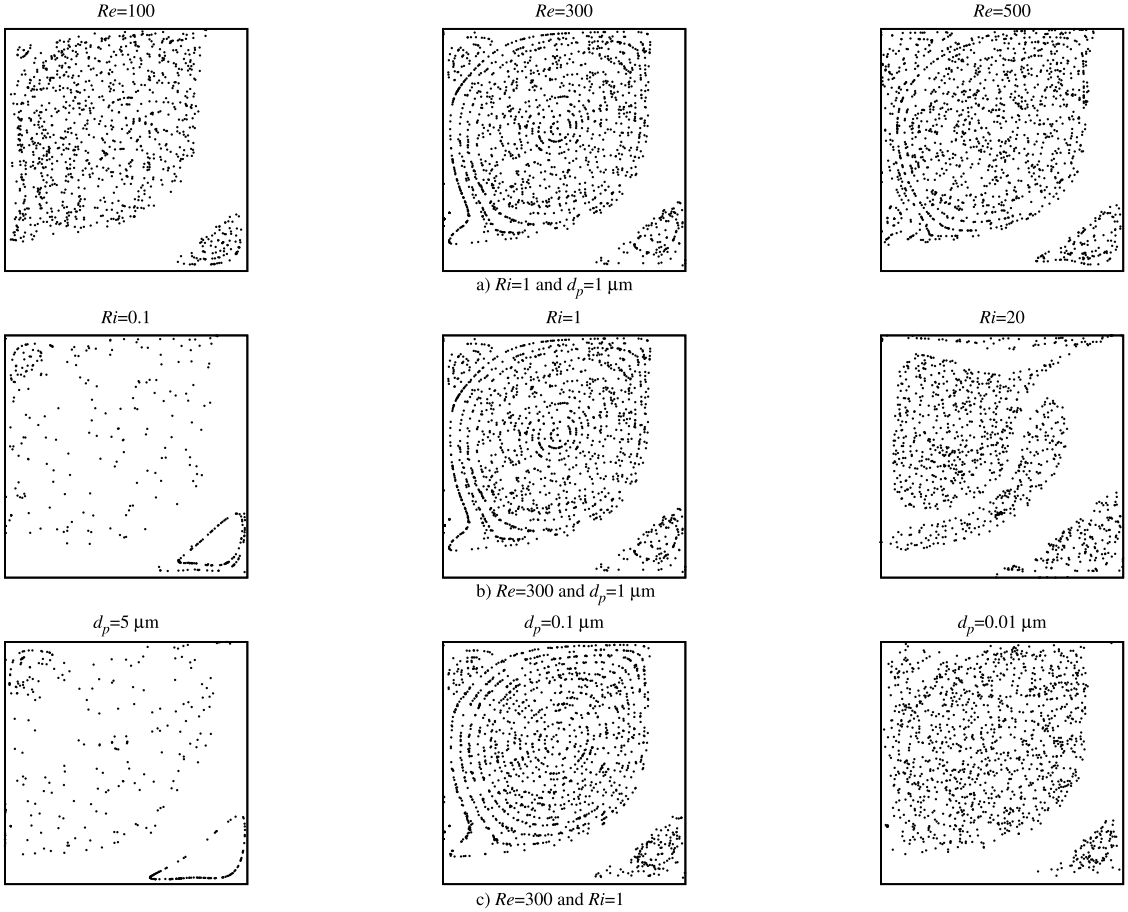

Fig. 11. Particle distributions in the cases of different Reynolds numbers, Richardson numbers and particle diameters for given parameters.

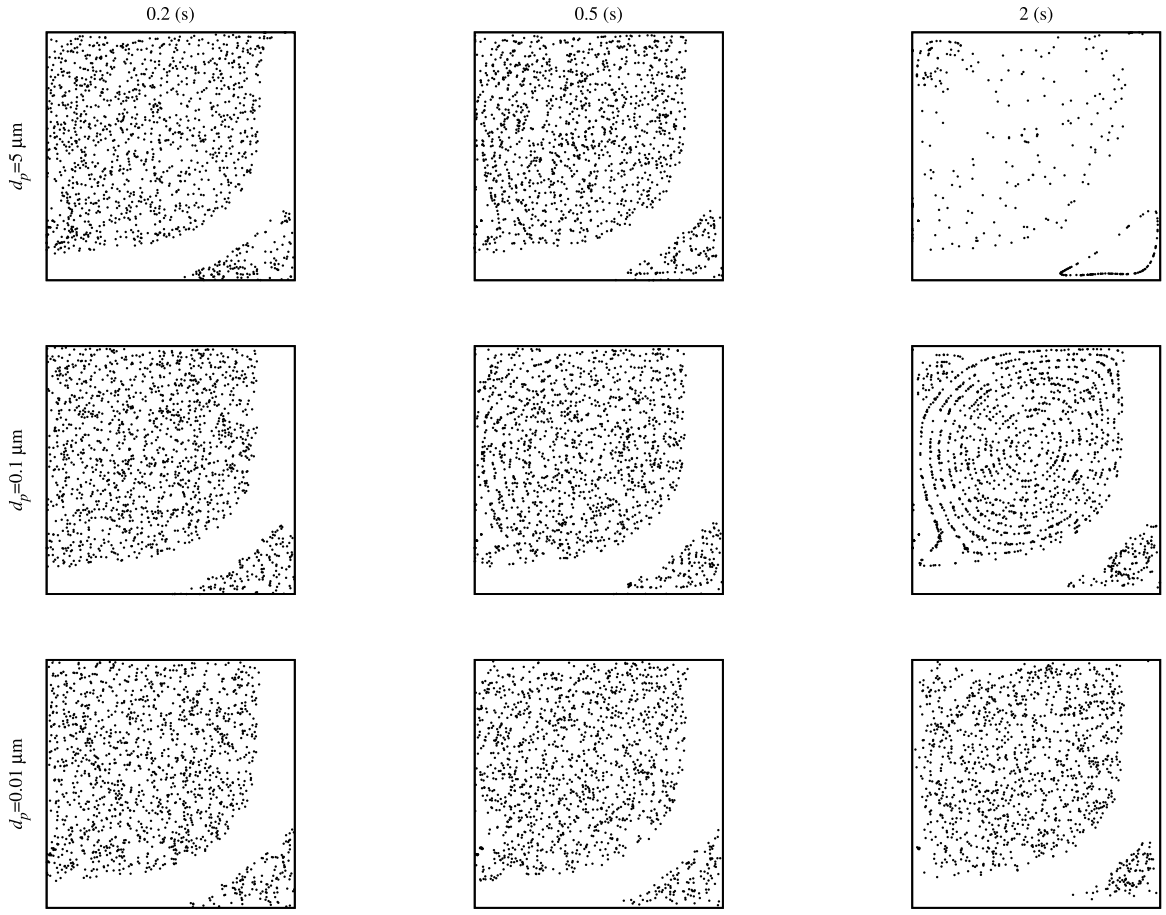

Fig. 12. Particle distributions at selected time snapshots for different particle diameters with $Re = 300$ and $Ri = 1$.

$$S_{gen} = \underbrace{\underbrace{\left[\left(\frac{\partial \Theta_f}{\partial X}\right)^2 + \left(\frac{\partial \Theta_f}{\partial Y}\right)^2\right]}_{HTI} + \underbrace{\chi\left[2\left(\frac{\partial U_f}{\partial X}\right)^2 + 2\left(\frac{\partial V_f}{\partial Y}\right)^2 + \left(\frac{\partial U_f}{\partial Y} + \frac{\partial V_f}{\partial X}\right)^2\right]}_{FFI}}_{S_{gen,f}}$$
$$+ \underbrace{\underbrace{\frac{T_0^2 L^2}{k_f(\Delta T)^2}\left[\sum_{n_p} \frac{1}{\delta \forall}\left(\frac{(T_p - T_f)^2}{T_0^2} h A_p\right)\right]}_{PHTI} + \underbrace{\frac{T_0^2 L^2}{k_f(\Delta T)^2}\left[\sum_{n_p} \frac{1}{\delta \forall}\left(\frac{1}{T_0} F_{tot} V_r\right)\right]}_{PFFI}}_{S_{gen,p}} \tag{25}$$

Box I.

Table 4
Comparison of the average Nusselt numbers with the inlet and outlet sizes $W = 0.25$.

Re	$S = 1.5$		$S = 2.5$		$S = 3.125$	
	Present	Saeidi & Khodadadi [12]	Present	Saeidi & Khodadadi [12]	Present	Saeidi & Khodadadi [12]
10	3.742	3.832	3.692	3.768	3.912	4.106
40	5.499	5.662	5.413	5.665	6.288	6.446
100	8.041	7.854	7.945	7.951	9.336	9.164
500	15.516	14.862	16.001	15.431	20.015	19.055

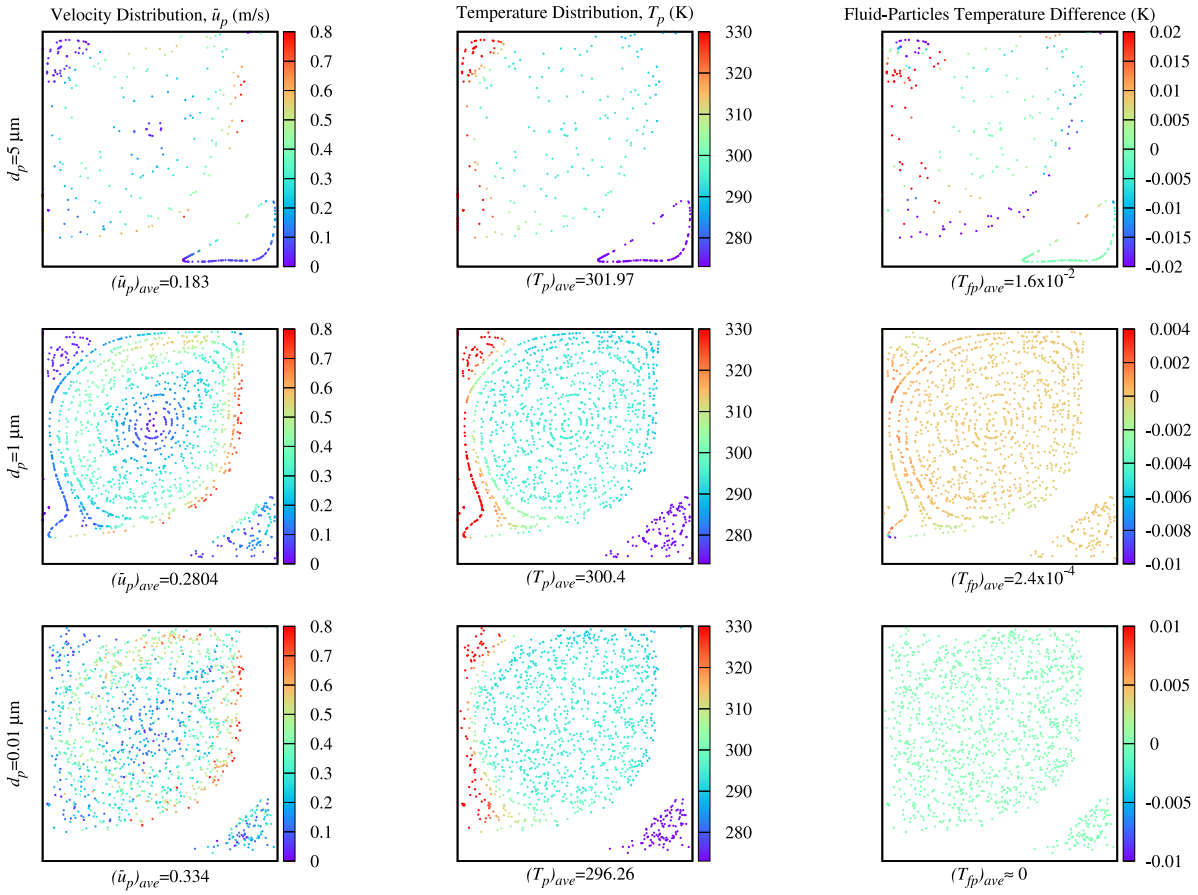

Fig. 13. Particle velocity, temperature and temperature difference between fluid and solid phases for different particle diameters with $Re = 300$ and $Ri = 1$.

Table 5
Average Nusselt number on the hot wall in the cases of various Reynolds numbers and Richardson numbers.

Ri	$Re = 50$	$Re = 100$	$Re = 300$	$Re = 500$
0.1	3.8096	5.0356	8.5906	12.2016
0.5	3.7796	4.9700	8.4598	12.0601
1	3.7403	4.8792	8.2803	11.8714
5	3.3809	4.0860	6.8595	9.2858
10	3.3822	4.2386	7.0608	9.7342
20	4.3070	5.9774	12.0138	15.7538

$$T_p^{(t+\Delta t)} = \left(T_f\right)^{(t)} + \left(T_p - T_f\right)^{(t)} \exp\left(-D\Delta t\right) \tag{29}$$

where

$$A_i = \rho_p \mathcal{V}_p$$
$$B_i = \left(\rho_p - \rho_f\right)\mathcal{V}_p g_i + F_{B,i} + F_{T,i}$$
$$C_i = f + L_i$$
$$L_x = 1.615\rho_f \nu_f^{0.5} d_p^2 \sqrt{\left|\frac{dv_f}{dx}\right|}\,\mathrm{sign}\left(\frac{dv_f}{dx}\right) \tag{30}$$
$$L_y = 1.615\rho_f \nu_f^{0.5} d_p^2 \sqrt{\left|\frac{du_f}{dy}\right|}\,\mathrm{sign}\left(\frac{du_f}{dy}\right)$$
$$D = \frac{6k_f}{\rho_p (c_p)_p d_p^2} Nu_p$$

The determination of the fluid velocity and temperature at particle position in the Lagrangian frame is necessary, therefore the bilinear function in Eq. (31) is used to interpolate the variables of fluid in Fig. 2 [73].

$$f(p) = f(Q_{11})\frac{(x_2 - x)(y_2 - y)}{(x_2 - x_1)(y_2 - y_1)} + f(Q_{21})\frac{(x - x_1)(y_2 - y)}{(x_2 - x_1)(y_2 - y_1)} + f(Q_{12})\frac{(x_2 - x)(y - y_1)}{(x_2 - x_1)(y_2 - y_1)} + f(Q_{22})\frac{(x - x_1)(y - y_1)}{(x_2 - x_1)(y_2 - y_1)} \tag{31}$$

The grid dependency test in Table 3 is carried out by examining the average Nusselt numbers on the hot vertical wall for five uniform mesh sizes. Also, Fig. 3 presents the non-dimensional temperature and vertical velocity distributions at middle height ($Y = 0.5$) with different mesh sizes, and a uniform mesh grid (82×82) is selected. The accuracy of the present FORTRAN code is validated by comparing with the results of Saeidi and Khodadadi [12] in the case of the forced convection in a square ventilating cavity. The key parameters are listed as: the non-dimensional width of the inlet and outlet ports W is 0.25, the different non-dimensional locations of the outlet port S are 1.5, 2.5 and 3.125, and $Re = 10$, 40, 100 and 500. The comparison of the average Nusselt numbers between the presented results and those of Saeidi and Khodadadi [12] is presented in Table 4. In Fig. 4, the experimental [65] and numerical [66] studies are compared with the present results for the variations of vertical and horizontal velocity profiles along the centerlines in the lid-driven cubic cavity for $Re = 400$. The variations of suspended particle fractions for $Ra = 10^5$ and the particles in the range of 10 µm to 0.01 µm are compared with those of Bagheri et al. [33] in Fig. 5. It is observed that there is a good agreement with the two studies. The accuracy of the particle trajectory is essential for this research. For this reason, the present numerical results are also compared to the experimental [67] and numerical [68]

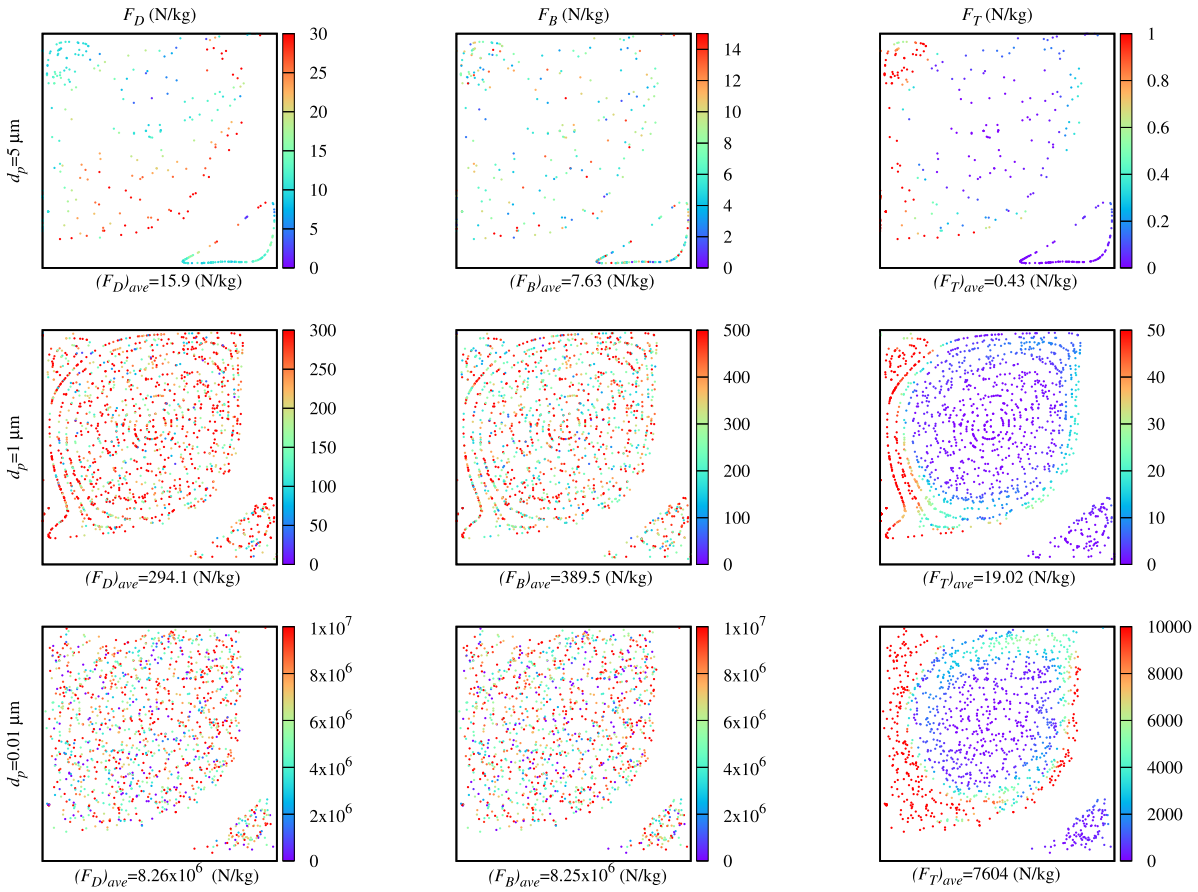

Fig. 14. Drag, Brownian and Thermophoretic forces of suspended particles for different particle diameters with $Re = 300$ and $Ri = 1$.

studies on the trajectory of the suspended solid particle in the lid-driven cavity flow in Fig. 6. The operating parameters of these studies are given as: the kinematic viscosity of the fluid is 37.2 mm^2/s, the specific gravity is 1.21, the cavity side is 10 cm, $Re = 470$, the diameter of the particle is 3 mm, the velocity of moving upper wall is 17.5 cm/s, and the densities of the fluid and the particle are nearly same. A very good agreement is observed between our result and these two experimental and numerical works. These comparisons provide evidence for the ability of the present code to analyze the proposed study.

4. Results and discussion

The results of laminar mixed convection in a vented cavity are presented taking into account the effects of various Reynolds numbers and Richardson numbers on the thermal and flow behaviors. Based on the second law of thermodynamics, entropy generation minimization is considered to examine the thermal design and optimization of this study. The findings of deposition and removal of particles in the range of 5 µm to 0.01 µm are demonstrated to understand the influences of mixed convection of airflow on the behaviors of particles . The velocity and temperature distributions of suspended particles tracked over 2 s are investigated using the Eulerian–Lagrangian approach with one-way coupling. It is introduced how the presence or absence of thermophoresis and Brownian forces affect the behavior of particles. In this study, some parameters are kept at a constant value; $Pr = 0.71$ and $a = L/10$.

Fig. 7 illustrates the streamlines distribution related to different Reynolds numbers and Richardson numbers in the square vented cavity. For $Ri = 0.1$ and 1, a primary counter-clockwise rotating vortex is observed above the main fluid stream while secondary clockwise vortices appear at the right bottom corner at a low Reynolds number. With rising the value of Reynolds number, the clockwise small cell is formed in the vicinity of the left top corner, and the main vortex grows in strength and size. The results obtained with $Re = 500$ show that the primary circular vortex becomes more dominant in the rest of cavity above incoming fluid flow, the stream function gets the maximum value in the cases of $Ri = 0.1$ and 1. The low Richardson numbers lead to create weak clockwise vortices above incoming stream flow in the vicinity of the inlet port for high Reynolds numbers. On the other hand, increasing Richardson number to 10 causes the primary recirculating vortex to shrink in size and a decrease in the maximum value of stream function and strength for all Reynolds numbers. Due to more buoyancy effect in the cavity at $Ri = 10$, the main vortex undergoes a change in shape from a circle to an elliptic, the clockwise rotating convective vortices at the left top corner get larger. At $Ri = 10$ and higher Reynolds number, the main recirculating vortex suppressed between these convective vortices and incoming stream flow transforms more elliptical shape and the small vortices located above incoming stream flow in the vicinity of the inlet section vanish. For all Reynolds numbers, the weak vortices occurring in the vicinity right bottom corner rise in size and the convective recirculating clockwise zone, which is gradually growing with Reynolds number at the left top corner, occupies more size inside the vented cavity in the cases of $Ri = 20$. One of significant results is that the increase in Richardson number to 20 causes the streamlines from incoming fluid flow to surround the elliptical vortex and large convective vortices. These streamlines move between these recirculation zones, then they arrive the outlet port traveling along the left and top wall. As expected, the surrounding effect is both reduced and confined by the increase in Reynolds number.

The temperature fields presented in Fig. 8 in terms of Reynolds numbers and Richardson numbers demonstrate that the increment in Reynolds number leads to a rise in the low temperature region for

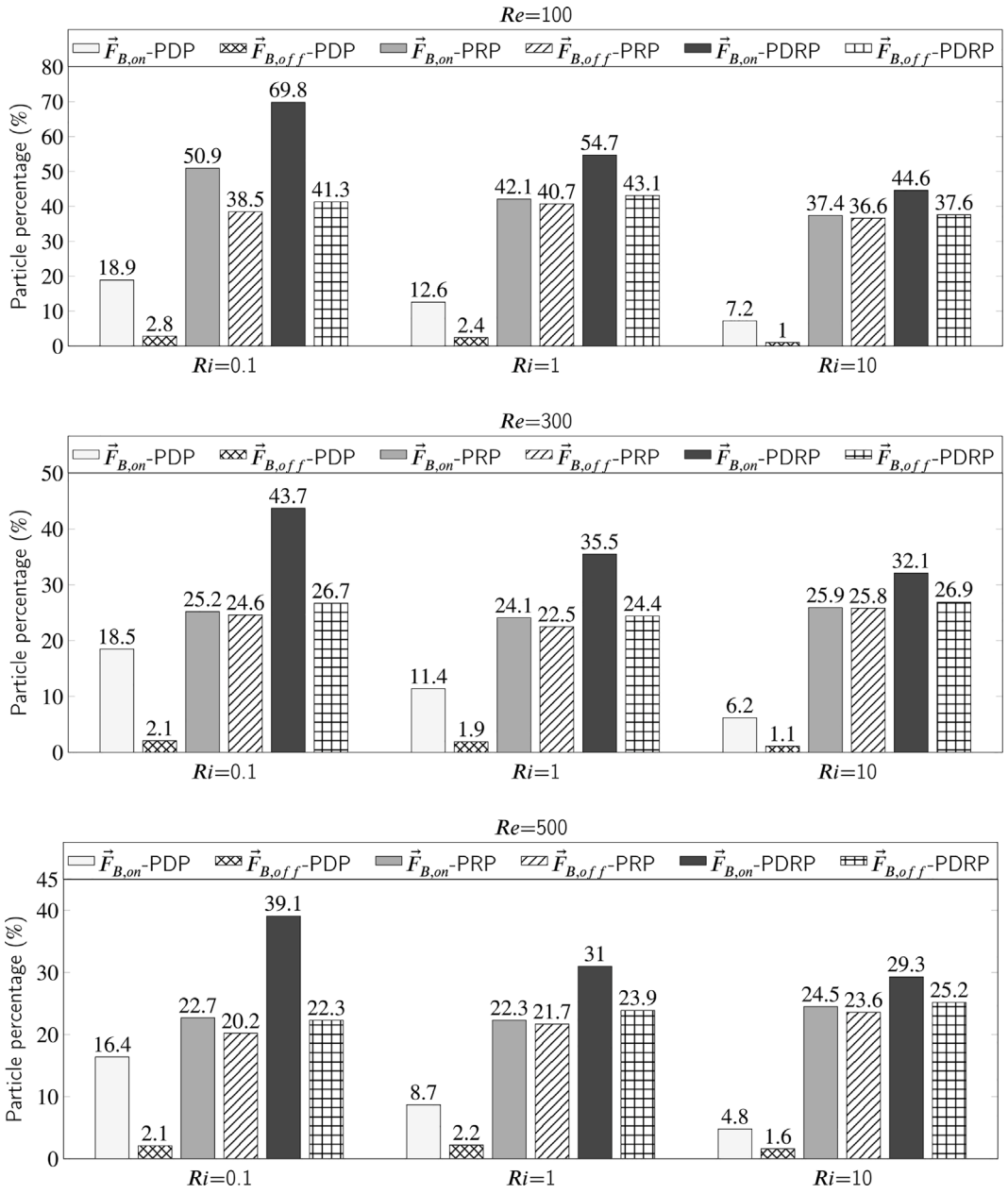

Fig. 15. Particle deposition percentage (PDP), particles removal percentage (PRP) and sum of both percentages (PDRP) for different Reynolds numbers in the absence and presence of Brownian random effect in the cases of $Ri = 0.1$, 1, 10 and $d_p = 0.01$ μm.

all Richardson numbers due to more effect of incoming cold fluid flow. Also, with augmentation of Reynolds number, higher temperature gradient and a thinner thermal boundary layer occur near the hot wall for given Richardson number. The convective interaction between the primary vortex and incoming fluid flow leads to high temperature gradient near the upper of inlet section, especially for high Reynolds number and low Richardson number. As the natural convection begins to dominate, the high temperature zone occupies more area in the upper of the main fluid stream, and the location of the maximum temperature gradient, close to the hot wall, is observed near the inlet port at $Ri = 10$. Also, it can be emphasized that the increase in Reynolds number with $Ri = 10$ causes the temperature fields to become stratified, and the heat transfer mechanism, carried out between the elliptic main vortex and the clockwise convective vortices beginning to grow on the left top corner, is more enhanced. With increasing the buoyancy effect, the temperature gradient becomes steeper and the isotherms are more stratified in the region above the main fluid stream at $Ri = 20$. Also, higher temperature gradient is observed at the right top corner for high Reynolds numbers with $Ri = 20$.

Table 5 gives the average Nusselt numbers on the hot wall for different Reynolds numbers and Richardson numbers in the range of 50–500 and 0.1–20, respectively. As Reynolds number increases, the average Nusselt number gets higher value for given Richardson number, and the heat transfer mechanism is enhanced near the hot wall. The increment in Richardson number leads to first decrease and then increase the average Nusselt number. Its maximum value is obtained for $Re = 500$ and $Ri = 20$ where the natural convection becomes more dominant. It is shown that the average Nusselt number on the hot wall takes a minimum value in the case of $Ri = 5$ for all Reynolds numbers.

As noted in Fig. 9, the results of the Particle Deposition Percentages (PDP), the Particle Removal Percentages (PRP) and the sum of Particle Deposition and Removal Percentages (PDRP) for particle sizes varying from 5 μm to 0.01 μm in diameter associated with two different Reynolds numbers and Richardson numbers are given. At $Re = 300$,

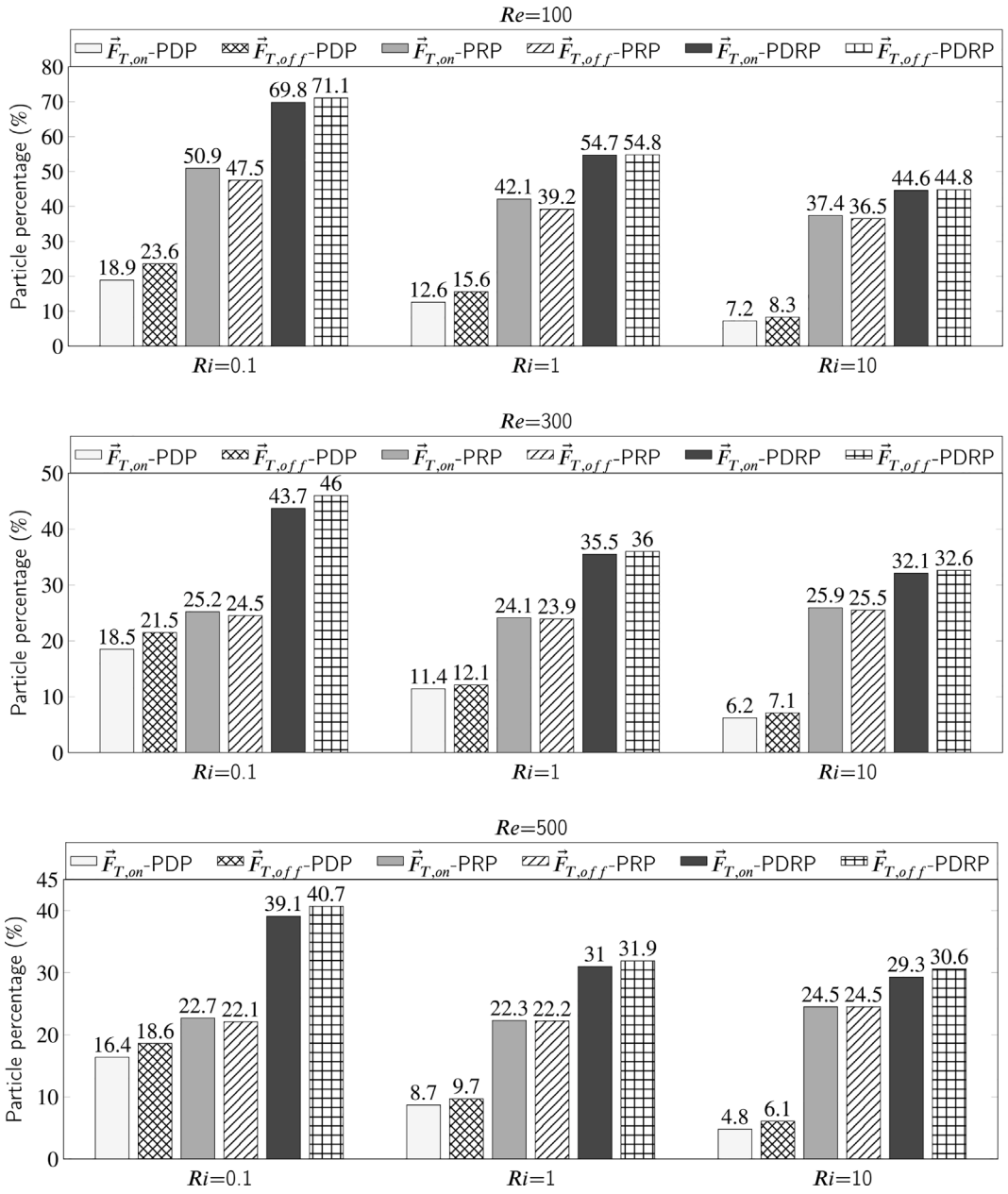

Fig. 16. Particle deposition percentage (PDP), particles removal percentage (PRP) and sum of both percentages (PDRP) for different Reynolds numbers in the absence and presence of thermophoretic effect in the cases of Ri = 0.1, 1, 10 and d_p = 0.01μm.

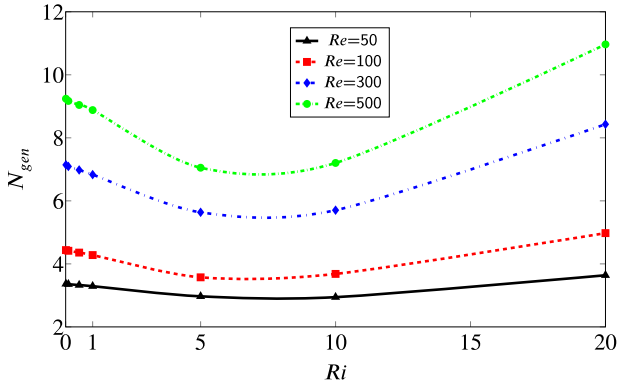

Fig. 17. The variation of total entropy number versus Richardson number for different Reynolds numbers.

500 and Ri = 0.1, a very small number of 5 μm particles remains in the cavity, while the deposition rate is greater than the removal rate. Since the inertia force of large particles is higher, the particles initially suspended in the corner vortices and the main vortex do not follow the fluid exactly, their position changes from the inside to the outside in the cells. The outward motion of 5 μm particles is in the form of a spiral trajectory inside the main vortex. As the intensity of this vortex cannot dominate over the inertial effect along with the gravity force, the particles move into the main fluid flow and are carried to the exit section. These particles deposit on the upper wall near the exit zone with a powerful main fluid stream, while a lower number of those is removed from the outlet port. It can be seen that the increase in the rate of suspended particle in the main cell and weak corner vortices is provided by the decrease in the inertial force and gravity effect in the case of Re = 300 and Ri = 0.1 for 1 μm particles. The total percentage of deposition and removal reduces, but the deposition rate is greater than that of 5 μm particles because more 1 μm particles are pushed

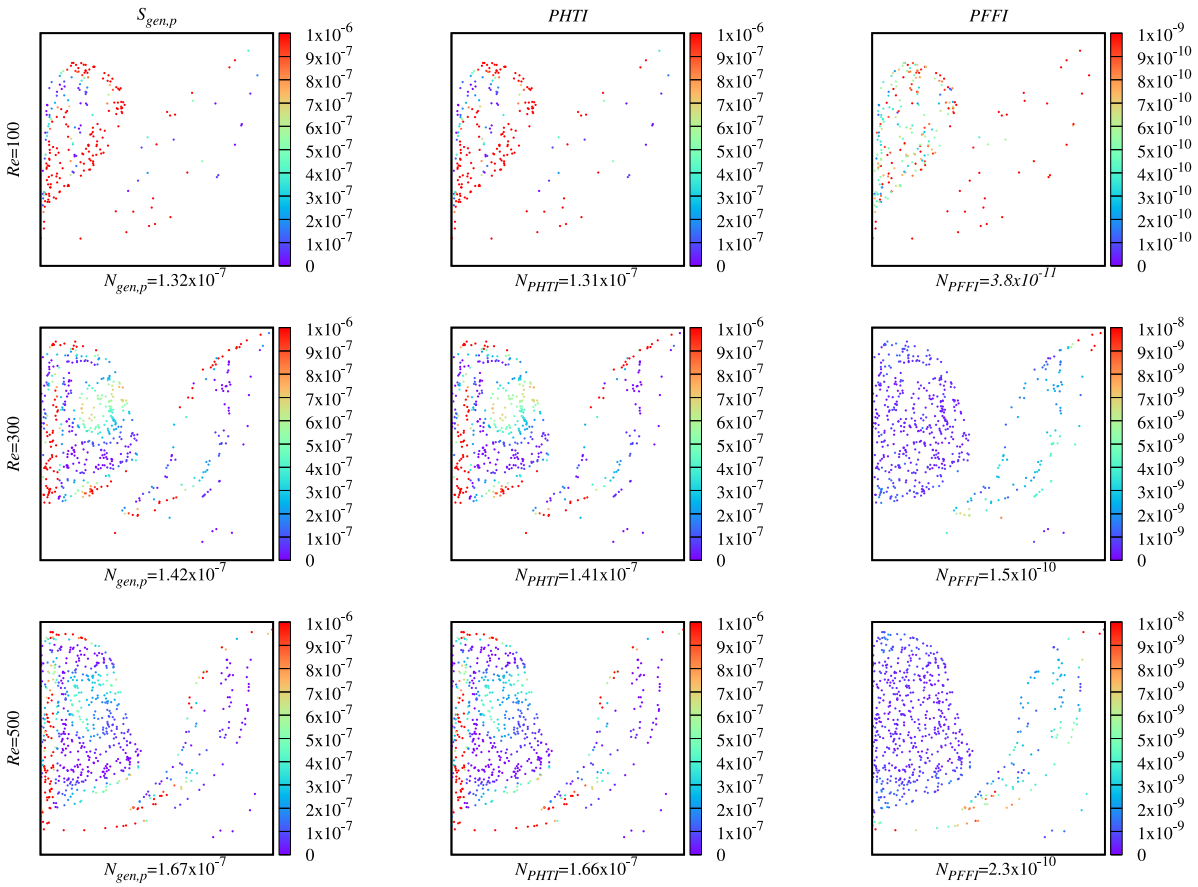

Fig. 18. Non-dimensional local entropy generations and total entropy generations due to heat transfer between solid particle and fluid phase and frictional total force for different Reynolds numbers with $Ri = 20$ and $d_p = 20\mu m$.

by the incoming fluid flow towards the top wall near the outlet port and deposit due to less gravity effect. The corner vortices and the main recirculating cell intensified by increasing Reynolds number to 500 achieve to trap the more 1 μm particles at $Ri = 0.1$. Both gravity and inertia effects on 0.1 μm particles are much less, therefore particles with small size, most of which are trapped in the primary vortex and corner vortices, follow streamlines. However, the random motions are more distinctly observed with the higher Brownian effect on particles with a diameter of 0.01 μm. This randomness increases the deposition on the walls and causes more particles to be pushed into the main fluid stream from the small vortices and large recirculating zone and the particle removal rate becomes higher value. As Reynolds number increases from 300 to 500, there is a decrease in the deposition and removal rates of particles with diameters of 0.1 μm and 0.01 μm at $Ri = 0.1$ since there are more powerful vortices trapping more particles. Due to the greater natural convection effect, the left upper weak clockwise vortices expand more, and the shape of the main recirculating cell changes from circular to elliptical. With weaker inertia effects caused by the natural convection effect, particle deposition rates become very small and a decrease in the particle removal rate is observed because the vortices and the primary elliptical shaped vortex have enough strength to capture and hold the particles. The Brownian effect brings about the highest particle deposition when the particle diameter is 0.01 μm at $Ri = 10$.

The results of the sum of Particle Deposition and Removal Fraction (PDRF) associated with different particle diameters, Reynolds numbers and Richardson numbers are given in Fig. 10. For $Re = 50$, 100 and 300, $Ri = 0.1$ where forced convection is more effective, the high inertia effect on 5 μm and 1 μm particles lead to higher PDRF, while the PDRF values of 5 μm and 0.01 μm particles at $Re = 500$ ve $Ri = 0.1$ take higher values due to in the presence of inertia and Brownian effects, respectively. Because there are strong vortices at $Re = 500$, when forced convection is very dominant, most 1 μm particles are trapped in rotating zones, unlike the cases of other Reynolds numbers. With rising Richardson number, first a decrease and then an increase in PDRF values of all particle diameters are observed. The minimum PDRF values of all particle sizes are calculated at $5 \leq Ri \leq 10$ for low Reynolds number while these values are observed at $1 \leq Ri \leq 10$ with higher Reynolds number. For given Reynolds number, the more suspended particles in the ventilating cavity are found at $Ri > 0.1$ for particles with diameters of 1 μm and 0.1 μm. In addition, the increment in Reynolds number allows more particles to be suspended.

The distribution of particles found in the vented cavity using the Lagrange tracking model is presented in Fig. 11 for different Reynolds numbers, Richardson numbers, and particle diameters. As seen in Fig. 11 (a), as strong cells occur with an increase in the Reynolds number, there is a decrease in the fraction of particles that move away from the center of recirculation zones and are trapped in the main fluid stream flow due to the inertia effect. An increase in the Reynolds number leads to a thinner thermal boundary layer on the hot wall and a decrease in the thermophoresis effect region. Therefore, more particles remain suspended near the left wall for higher Reynolds number.

As shown in Fig. 11 (b), the locations of the particles for different Richardson numbers are presented at $Re = 300$ and $d_p = 1\mu m$. At $Ri = 0.1$, where there is a high forced convection effect, particles are pushed toward the incoming fluid flow from the primary vortex and removed from the outlet section. As a result, the fraction of suspended particles is very low. With the decreasing inertia effect on the 1 μm particle associated with the growing the natural convection effect, the particles follow the streamlines with a slight deviation. There are lower

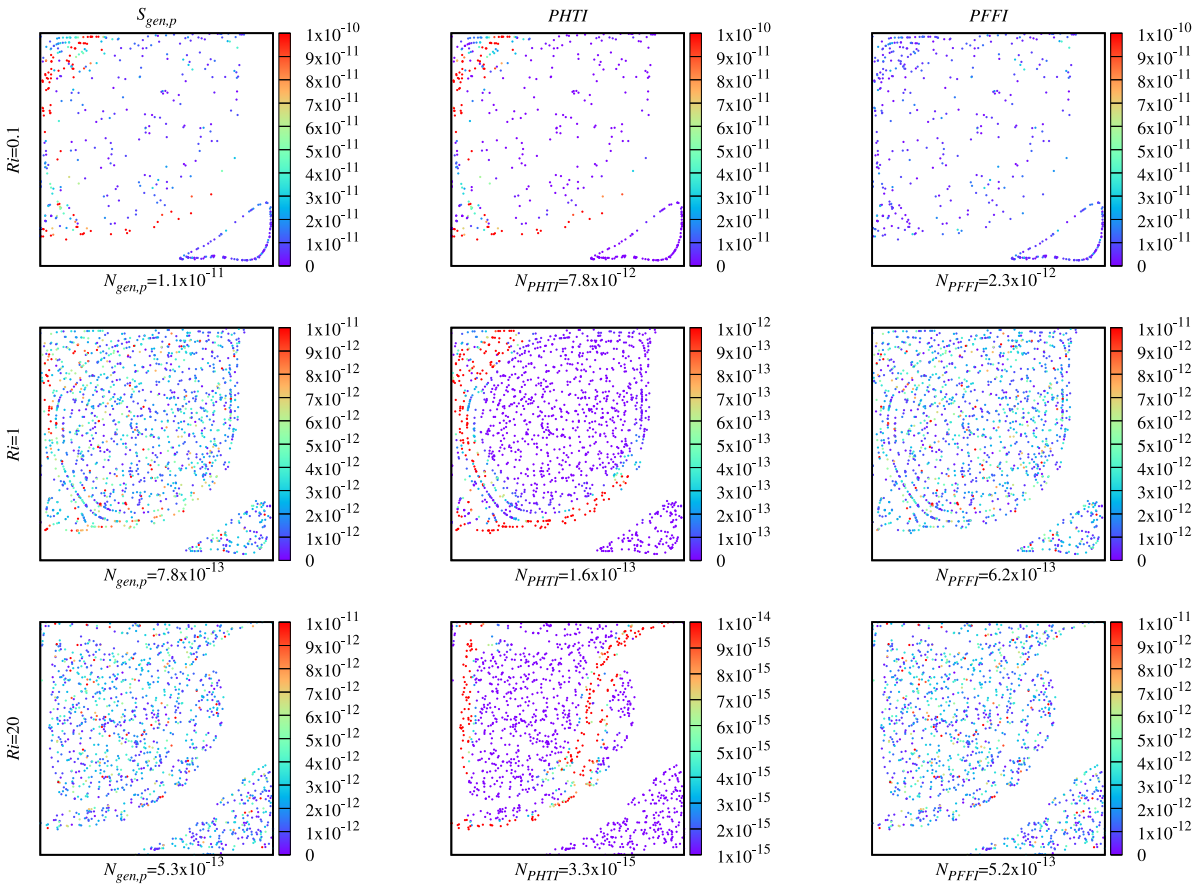

Fig. 19. Non-dimensional local entropy generations and total entropy generations due to heat transfer between solid particle and fluid phase and frictional total force for different Richardson numbers with $Re = 500$ and $d_p = 1\mu m$.

suspended particles in the case of $Ri = 20$ compared to $Ri = 1$ as streamlines from the incoming stream flow move further inside the vented cavity. Fig. 11 (c) shows that there are greater inertia and gravity effects on the distribution of large particles. Because of the effects of low inertia and gravity, the trajectories of 0.1 μm particles are dependent on the flow structure. The higher Brownian effect causes 0.01 μm particles to be distributed more irregularly and randomly than 0.1 μm particles.

The selected snapshots of particles locations for three particle diameters are demonstrated in Fig. 12 at $Re = 300$ and $Ri = 1$. d_p = 5 μm, 0.1 μm and 0.01 μm particles initially located at the path of incoming fluid flow are deposited and removed in the vented cavity at the beginning of particle tracking. Due to the inertial force, the number of 5 μm particles remaining in the corner vortices and the primary cell are gradually reduced and are discharged by the hydrodynamics effect of the incoming fluid flow from the outlet and deposited on the upper wall. 0.1 μm particles placed in the vicinity of the left wall are pushed into the primary vortex and kept away from the left wall due to the high thermophoretic effect. After a while, the quasi-equilibrium regions in which 0.1 μm particles move along the streamlines develop. Increasing Brownian random effect leads to more 0.01 μm particle deposition on the left and top walls in time. Eventually, the number of suspended 0.01 μm particles is less than that of 0.1 μm particles.

The velocity and temperature distributions of the particles remaining suspended and the temperature differences between the fluid and particles are presented in Fig. 13 by solving the equations of particle motion and particle energy equation in the Lagrangian frame for different particle diameters. The results of the velocity distributions indicate that there are few 5 μm particles with high velocity. In particular, low-velocity particles are relatively numerous in weak two recirculation zones at corners. For this reason, average 5 μm particle velocity ($(\overline{u}_p)_{ave}$) is low. As the particle size decreases, an increase in the average particle velocity and high-velocity particle numbers with small diameter are observed with an ever-decreasing inertia and gravity effects and an ever-increasing Brownian random effect. As expected, low-velocity particles are observed in weak corner vortices and the center of the primary circulating vortex, while particles with high velocity are found in the region where the primary vortex is adjacent to the incoming fluid flow. The average temperature values of suspended particles, $(\overline{T}_p)_{ave}$, tend to diminish with reducing particle size. The suspended particles occupying near the hot left wall get higher temperature value, whereas particles with low temperature remain in the vicinity of the right bottom corner. Considering the temperature differences, it is observed that the temperatures of 5 μm particles are greater than the fluid temperature in the upper left corner and in the region where the main vortex is adjacent to the incoming fluid flow. While the fluid temperature is greater than the particle temperature in locations close to the left wall, the temperature differences in other regions are close to zero. The temperature differences between the 1 μm particles and fluid are smaller compared to the results of 5 μm particles. The 1 μm particle temperature is slightly higher than that of the fluid in front of the inlet section, while the fluid temperature is slightly higher than that of the 1 μm particle near the left wall. The temperature differences are very low in the whole vented cavity for 1 μm particles. 0.01 μm particle temperature and fluid temperature are almost the same and temperature differences are nearly zero inside the whole system. Similarly, as the particle size decreases, the value of $(T_{fp})_{ave}$ gets smaller and approaches zero. Consequently, the local thermal equilibrium between small solid particles and fluid phase is observed.

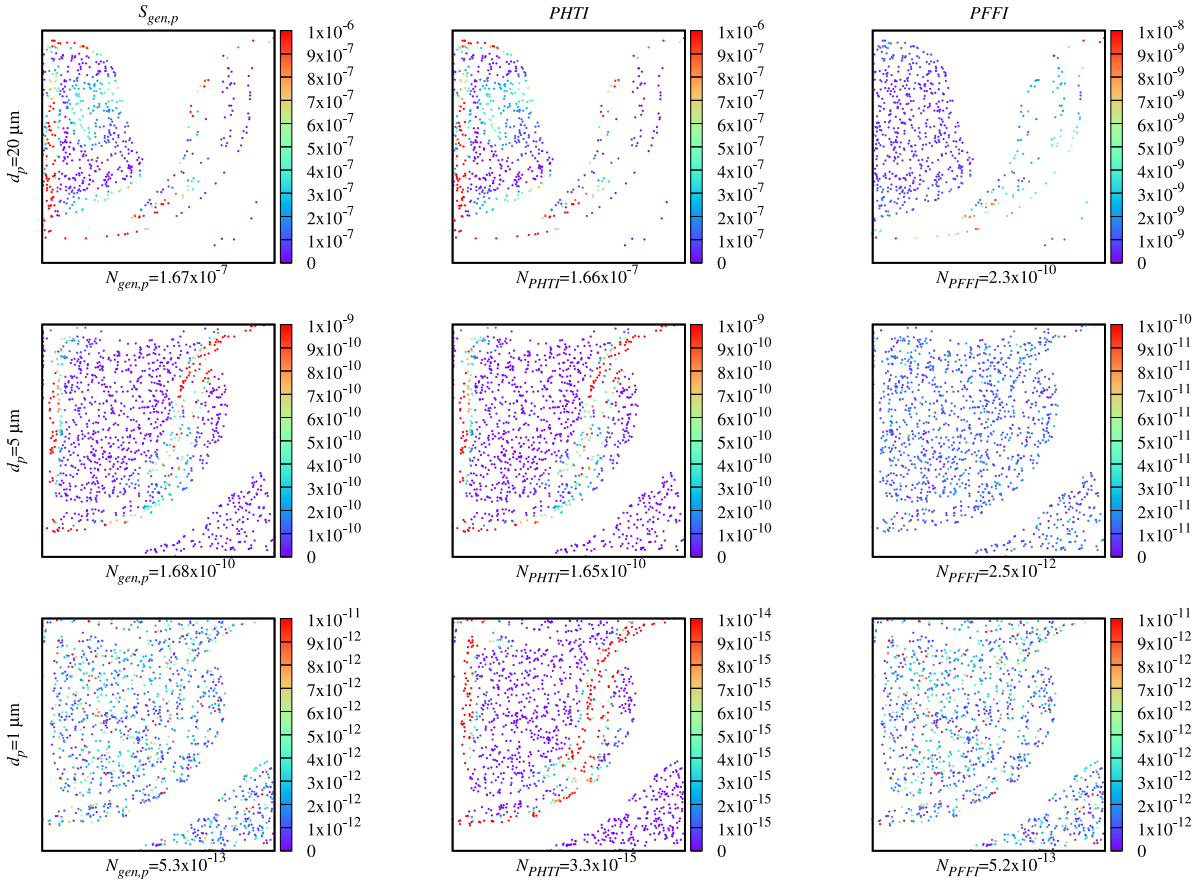

Fig. 20. Non-dimensional local entropy generations and total entropy generations due to heat transfer between solid particle and fluid phase and frictional total force for different particle diameters with $Re = 500$ and $Ri = 20$.

In Fig. 14, the distributions of drag, Brownian and thermophoresis forces (N/kg) of particles with different sizes and their averages (N/kg) are illustrated. All these forces per unit mass increase with decreasing particle diameter. The thermophoresis forces on the left wall, where the temperature gradients are higher, push the particles toward recirculating zones and reduce the deposition on the left wall. The thermophoretic effect, which tends to push particles remaining in the outer region of the primary vortex to the incoming fluid flow, occurs due to the medium temperature gradient between the primary vortex and the incoming fluid flow.

Particle Deposition Percentage (PDP) and Particle Removal Percentage (PRP) are demonstrated in the absence and presence of the Brownian effect in Fig. 15 for 0.01 μm particles. In the absence of the Brownian effect for all Reynolds numbers and Richardson numbers, the deposition rate drops very significantly, especially on the top and left wall where the particles are close. With the neglected Brownian effect, the particle removal rate decreases very slightly, except for the case with $Re = 100$ and $Ri = 0.1$, where there is a significant decline in the value of PRP.

In Fig. 16, the deposition and removal of 0.01 μm particles are examined with regard to the presence and absence of thermophoretic effect. The lack of thermophoretic force leads to further deposition on the left wall. By neglecting the thermophoretic effect, the number of particles pushed to incoming fluid flow and the particles removal rate are reduced slightly.

In Fig. 17, the variation of total entropy generation for six Richardson numbers is presented considering the effects of forced convection and buoyancy force. Due to the low order of magnitude of irreversibility distribution and low particle volume fraction, the fluid friction irreversibility and contribution of particles remaining suspended in the enclosure to entropy generation are very small, and the irreversibility due to heat transfer is more dominant. For given Reynolds number, increasing Richardson number leads first to a decrease, and then to an increment in the total entropy generation. It gets higher values when forced convection or natural convection predominates in the vented cavity. Owing to a more convective effect, increasing total entropy generation occurs as Reynolds number becomes higher with the given Richardson number. While the minimum total entropy generation is obtained at $Ri = 5$ for high Reynolds numbers, its minimum value is observed at $Ri = 10$ in the case of $Re = 50$.

When the irreversibilities stemming from the presence of particles are examined in detail as seen in Figs. 18–20, it is pointed out that this investigation can be useful in terms of thermal design and optimization of the systems where the behaviors of particles are more important, although the results get lower values in this study due to low particle volume fraction. Fig. 18 displays the irreversibility arising from the presence of particles in terms of various Reynolds numbers at $Ri = 20$ and $d_p = 20\mu m$. The increment in Reynolds number leads to higher local entropy generation due to heat transfer exchange between particle and fluid ($PHTI$) and frictional total force ($PFFI$), therefore the local ($S_{gen,p}$) and total entropy generations ($N_{gen,p}$) for the solid particles are higher. It is shown in Fig. 19 that a decrease in entropy generation resulting from the presence of particles is caused by the rising Richardson number with $Re = 500$ and $d_p = 1\mu m$. Fig. 20 presents the change in $S_{gen,p}$ and $N_{gen,p}$ with regard to different particle diameters at $Re = 500$ and $Ri = 20$. The large particles result in the growth of entropy generation due to heat transfer between particle and fluid surrounding it and frictional total force acting on a particle.

5. Conclusion

The numerical investigation of mixed convection and entropy generation of airflow in a ventilating square cavity is carried out in terms of heat transfer mechanism and flow structure. The relationship between the deposition and removal mechanisms and the forces acting on particles are discussed under different thermal boundary conditions of mixed convective heat transfer. The results of this study on mixed convection can provide a viewpoint for the distribution of hazardous particles, such as radioactive dust, viruses and contaminants, in a vented enclosure. The irreversibilities due to interaction between fluid–solid particles are also considered in the analysis of entropy generation at various shear and buoyancy forces. This approach can be helpful in terms of thermal design and optimization for some applications involving solid particles, such as solar thermal systems, thermal energy storage, and heat exchangers.

The influences of airflow entering from the inlet port for different cases related to Reynolds number and Richardson number on the behaviors of particles a diameter in the range of 5 μm to 0.01 μm are emphasized by considering the various forces acting on the particles. The effects of mixed convection on the particles deposited on the wall and removed from the exit section are investigated in detail considering thermal behavior and flow structure in the vented cavity. The entropy generation for fluid phase and solid particle is analyzed with respect to natural convection and forced convection. The outcomes of this study can be summarized as follows:

- For high Reynolds numbers and low Richardson numbers, stronger cells are formed, while the size and strength of the primary vortex are reduced due to the buoyancy effect with high Richardson numbers. Higher Reynolds number leads to the enhancement of heat transfer and greater temperature gradient on the hot left wall with lower or higher Richardson numbers.
- The maximum heat transfer rate is observed in the case of higher Reynolds and Richardson numbers whereas it gets a lower value at $Ri = 5$.
- The inertia and gravity effects play an essential role in the deposition and removal of large-scale particles, while the Brownian force significantly changes the behavior of particles with a small diameter.
- The high suspended particle rate is observed in the flow structure and thermal fields of the system in which the entropy generation number and the average Nusselt number get a minimum value.
- As the buoyancy effect begins to increase, an increase in the rate of suspended particles occurs for given constant parameters, while there is a decrease in this rate due to the more dominant buoyancy effect at $Ri = 20$.
- The Brownian force is significantly dominant in the deposition and removal rates while the thermophoretic effect has a more important role in particle deposition than particle removal.
- The cases where entropy generation is minimum are determined. Meanwhile, more dominant natural or forced convection brings about the higher total entropy generation. Even though the total entropy generation arising from the presence of solid particles ($N_{gen,p}$) is lower than the value of $N_{gen,f}$ in this study, the analysis of irreversibility due to heat transfer between particle and fluid and frictional total force acting on a particle can be beneficial to the thermal design of a system where the effects of particle motions are vital.

Declaration of competing interest

The authors declare that they have no known competing financial interests or personal relationships that could have appeared to influence the work reported in this paper.

Data availability

No data was used for the research described in the article.

References

[1] C. Ophoff, N. Ozalp, D. Moens, A numerical study on particle tracking and heat transfer enhancement in a solar cavity receiver, Appl. Therm. Eng. 180 (2020) 115785.
[2] M. Amiraslanpour, J. Ghazanfarian, H. Nabaei, M.H. Taleghani, Evaluation of laminar airflow heating, ventilation, and air conditioning system for particle dispersion control in operating room including staffs: A non-Boussinesq Lagrangian study, J. Build. Phys. 45 (2) (2021) 236–264.
[3] Y. Yan, X. Li, X. Fang, P. Yan, J. Tu, Transmission of COVID-19 virus by cough-induced particles in an airliner cabin section, Eng. Appl. Comput. Fluid Mech. 15 (1) (2021) 934–950.
[4] E. Kosari, K. Vafai, Transport and dynamic analysis of magnetic nanoparticles in brain microvascular vessels, Phys. Fluids 33 (8) (2021) 081907.
[5] A. Albojamal, K. Vafai, Analysis of particle deposition of nanofluid flow through porous media, Int. J. Heat Mass Transfer 161 (2020) 120227.
[6] J. Tu, K. Inthavong, G. Ahmadi, Computational Fluid and Particle Dynamics in the Human Respiratory System, Springer Science & Business Media, 2012.
[7] J.-X. Wang, X. Cao, Y.-P. Chen, An air distribution optimization of hospital wards for minimizing cross-infection, J. Clean. Prod. 279 (2021) 123431.
[8] M. Abuhegazy, K. Talaat, O. Anderoglu, S.V. Poroseva, Numerical investigation of aerosol transport in a classroom with relevance to COVID-19, Phys. Fluids 32 (10) (2020) 103311.
[9] M. Liu, J. Liu, Q. Cao, X. Li, S. Liu, S. Ji, C.-H. Lin, D. Wei, X. Shen, Z. Long, et al., Evaluation of different air distribution systems in a commercial airliner cabin in terms of comfort and COVID-19 infection risk, Build. Environ. 208 (2022) 108590.
[10] Q. Cao, M. Liu, X. Li, C.-H. Lin, D. Wei, S. Ji, T.T. Zhang, Q. Chen, Influencing factors in the simulation of airflow and particle transportation in aircraft cabins by CFD, Build. Environ. 207 (2022) 108413.
[11] F. Wang, R. You, T. Zhang, Q. Chen, Recent progress on studies of airborne infectious disease transmission, air quality, and thermal comfort in the airliner cabin air environment, Indoor Air 32 (4) (2022) e13032.
[12] S. Saeidi, J. Khodadadi, Forced convection in a square cavity with inlet and outlet ports, Int. J. Heat Mass Transfer 49 (11–12) (2006) 1896–1906.
[13] K. Khanafer, S. Aithal, K. Vafai, Mixed convection heat transfer in a differentially heated cavity with two rotating cylinders, Int. J. Therm. Sci. 135 (2019) 117–132.
[14] E. Sourtiji, S. Hosseinizadeh, M. Gorji-Bandpy, D. Ganji, Heat transfer enhancement of mixed convection in a square cavity with inlet and outlet ports due to oscillation of incoming flow, Int. Commun. Heat Mass Transfer 38 (6) (2011) 806–814.
[15] A.J. Chamkha, S.H. Hussain, Q.R. Abd-Amer, Mixed convection heat transfer of air inside a square vented cavity with a heated horizontal square cylinder, Numer. Heat Transf. A Appl. 59 (1) (2011) 58–79.
[16] F. Selimefendigil, H.F. Öztop, Numerical investigation and dynamical analysis of mixed convection in a vented cavity with pulsating flow, Comput. & Fluids 91 (2014) 57–67.
[17] S.K. Gupta, D. Chatterjee, B. Mondal, Investigation of mixed convection in a ventilated cavity in the presence of a heat conducting circular cylinder, Numer. Heat Transf. A Appl. 67 (1) (2015) 52–74.
[18] N. Biswas, P.S. Mahapatra, N.K. Manna, Mixed convection heat transfer in a grooved channel with injection, Numer. Heat Transf. A Appl. 68 (6) (2015) 663–685.
[19] G. Yang, J. Wu, Conjugate mixed convection in the entrance region of a symmetrically heated vertical channel with thick walls, Int. J. Therm. Sci. 98 (2015) 245–254.
[20] I.I. Nosonov, M.A. Sheremet, Conjugate mixed convection in a rectangular cavity with a local heater, Int. J. Mech. Sci. 136 (2018) 243–251.
[21] M.A. Ismael, H.F. Jasim, Role of the fluid-structure interaction in mixed convection in a vented cavity, Int. J. Mech. Sci. 135 (2018) 190–202.
[22] F. García, C. Treviño, J. Lizardi, L. Martínez-Suástegui, Numerical study of buoyancy and inclination effects on transient mixed convection in a channel with two facing cavities with discrete heating, Int. J. Mech. Sci. 155 (2019) 295–314.
[23] L. Nasseri, D.E. Ameziani, O. Rahli, R. Bennacer, Numerical study of mixed convection in a ventilated square enclosure with the lattice Boltzmann method, Numer. Heat Transf. A Appl. 75 (10) (2019) 674–689.
[24] Z. Younsi, L. Koufi, H. Naji, Numerical study of the effects of ventilated cavities outlet location on thermal comfort and air quality, Internat. J. Numer. Methods Heat Fluid Flow (2019).
[25] K. Ezzaraa, A. Bahlaoui, I. Arroub, A. Raji, M. Hasnaoui, M. Naïmi, Radiation effect on mixed convection cooling in a ventilated horizontal cavity with multiple ports, Int. J. Mech. Sci. 153 (2019) 310–320.

[26] G. Rajamohan, N. Ramesh, P. Kumar, Mixed convection and radiation studies on thermally developing laminar flow in a horizontal square channel with variable side heated wall, Int. J. Therm. Sci. 140 (2019) 298–307.
[27] H.A. Dhahad, G.F. Al-Sumaily, L.J. Habeeb, M.C. Thompson, The cooling performance of mixed convection in a ventilated enclosure with different ports configurations, J. Heat Transfer 142 (12) (2020).
[28] L. Lukose, T. Basak, A comprehensive review on mixed convection for various patterns of kinematically and thermally induced scenarios within cavities, Internat. J. Numer. Methods Heat Fluid Flow (2021).
[29] R. Velkennedy, J.J. Nisrin, K. Kalidasan, P. Rajeshkanna, Numerical investigation of convective heat transfer in a rectangular vented cavity with two outlets and cold partitions, Int. Commun. Heat Mass Transfer 129 (2021) 105659.
[30] O. Prakash, S. Singh, Experimental and numerical study of mixed convection with surface radiation heat transfer in an air-filled ventilated cavity, Int. J. Therm. Sci. 171 (2022) 107169.
[31] F. Mebarek-Oudina, H. Laouira, A.K. Hussein, M. Omri, A. Abderrahmane, L. Kolsi, U. Biswal, Mixed Convection inside a Duct with an Open Trapezoidal Cavity Equipped with Two Discrete Heat Sources and Moving Walls, Mathematics 10 (6) (2022) 929.
[32] M. Akbar, M. Rahman, S. Ghiaasiaan, Particle transport in a small square enclosure in laminar natural convection, J. Aerosol Sci. 40 (9) (2009) 747–761.
[33] G. Bagheri, M. Salmanzadeh, V. Golkarfard, G. Ahmadi, Simulation of solid particles behavior in a heated cavity at high Rayleigh numbers, Aerosol Sci. Technol. 46 (12) (2012) 1382–1391.
[34] L. Ding, J. Fung, S. Seepana, A. Lai, Numerical study on particle dispersion and deposition in a scaled ventilated chamber using a lattice Boltzmann method, J. Aerosol Sci. 47 (2012) 1–11.
[35] V. Golkarfard, S.G. Nasab, A. Ansari, G. Bagheri, Numerical investigation on deposition of solid particles in a lid-driven square cavity with inner heated obstacles, Adv. Powder Technol. 23 (6) (2012) 736–743.
[36] V. Golkarfard, P. Talebizadeh, Numerical comparison of airborne particles deposition and dispersion in radiator and floor heating systems, Adv. Powder Technol. 25 (1) (2014) 389–397.
[37] F. Garoosi, M.R. Safaei, M. Dahari, K. Hooman, Eulerian–Lagrangian analysis of solid particle distribution in an internally heated and cooled air-filled cavity, Appl. Math. Comput. 250 (2015) 28–46.
[38] V. Ansari, A.S. Goharrizi, S. Jafari, B. Abolpour, Numerical study of solid particles motion and deposition in a filter with regular and irregular arrangement of blocks with using lattice Boltzmann method, Comput. & Fluids 108 (2015) 170–178.
[39] K. Inthavong, L. Tian, J. Tu, Lagrangian particle modelling of spherical nanoparticle dispersion and deposition in confined flows, J. Aerosol Sci. 96 (2016) 56–68.
[40] M. Mahdavi, M. Sharifpur, J. Meyer, Discrete modelling of nanoparticles in mixed convection flows, Powder Technol. 338 (2018) 243–252.
[41] Z. Yin, F. Bao, C. Tu, Y. Hua, R. Tian, Numerical and experimental studies of heat and flow characteristics in a laminar pipe flow of nanofluid, J. Exp. Nanosci. 13 (1) (2018) 82–94.
[42] Z. Han, Z. Xu, X. Yu, A. Sun, Y. Li, Numerical simulation of ash particles deposition in rectangular heat exchange channel, Int. J. Heat Mass Transfer 136 (2019) 767–776.
[43] P. Talebizadehsardari, H. Rahimzadeh, G. Ahmadi, K. Inthavong, M.M. Keshtkar, M. Moghimi, Nano-particle deposition in laminar annular pipe flows, Adv. Powder Technol. 31 (8) (2020) 3134–3143.
[44] A. Alsabery, A. Hajjar, M. Sheremet, M. Ghalambaz, I. Hashim, Impact of particles tracking model of nanofluid on forced convection heat transfer within a wavy horizontal channel, Int. Commun. Heat Mass Transfer 122 (2021) 105176.
[45] H. Lu, Y. Quan, A CFD study of particle deposition in three-dimensional heat exchange channel based on an improved deposition model, Int. J. Heat Mass Transfer 178 (2021) 121633.
[46] A. Jahanbin, G. Semprini, Integrated effects of the heat recovery ventilation and heat source on decay rate of indoor airborne particles: A comparative study, J. Build. Eng. 50 (2022) 104156.
[47] P. Biswal, T. Basak, Entropy generation vs energy efficiency for natural convection based energy flow in enclosures and various applications: a review, Renew. Sustain. Energy Rev. 80 (2017) 1412–1457.
[48] A. Bejan, Entropy Generation Through Heat and Fluid Flow, vol. 1, Wiley New York, 1982.
[49] U. Narusawa, The second-law analysis of mixed convection in rectangular ducts, Heat Mass Transf. 37 (2) (2001) 197–203.
[50] C.K. Chen, H.Y. Lai, C.C. Liu, Numerical analysis of entropy generation in mixed convection flow with viscous dissipation effects in vertical channel, Int. Commun. Heat Mass Transfer 38 (3) (2011) 285–290.
[51] G. Yang, J. Wu, Entropy generation in a rectangular channel of buoyancy opposed mixed convection, Int. J. Heat Mass Transfer 86 (2015) 809–819.
[52] A.K. Hussein, Entropy generation due to the transient mixed convection in a three-dimensional right-angle triangular cavity, Int. J. Mech. Sci. 146 (2018) 141–151.
[53] N. Gupta, A.K. Nayak, Activity of buoyancy convection and entropy generation in a parallelogrammic shaped mixed displacement ventilated system, Int. J. Therm. Sci. 137 (2019) 86–100.
[54] O. Çiçek, A.C. Baytaş, Conjugate forced convection in a semi-cylindrical cavity with entropy generation, Internat. J. Numer. Methods Heat Fluid Flow (2019).
[55] O. Çiçek, A.C. Baytaş, Local thermal non-equilibrium conjugate forced convection and entropy generation in an aircraft cabin with air channel partially filled porous insulation, Aircr. Eng. Aerosp. Technol. (2021).
[56] H. Hamzah, C. Canpolat, L.M. Jasim, B. Sahin, Hydrothermal index and entropy generation of a heated cylinder placed between two oppositely rotating cylinders in a vented cavity, Int. J. Mech. Sci. 201 (2021) 106465.
[57] F. Selimefendigil, H.F. Oztop, Mixed convection and entropy generation of nanofluid flow in a vented cavity under the influence of inclined magnetic field, Microsyst. Technol. 25 (12) (2019) 4427–4438.
[58] M. Benzema, Y.K. Benkahla, N. Labsi, S.-E. Ouyahia, M. El Ganaoui, Second law analysis of MHD mixed convection heat transfer in a vented irregular cavity filled with Ag–MgO/water hybrid nanofluid, J. Therm. Anal. Calorimetry 137 (3) (2019) 1113–1132.
[59] O. Çiçek, A.F. Baytaş, A.C. Baytaş, Entropy generation of mixed convection of SWCNT–water nanofluid filled an annulus with a rotating cylinder and porous lining under LTNE, Internat. J. Numer. Methods Heat Fluid Flow (2020).
[60] A. Li, G. Ahmadi, Dispersion and deposition of spherical particles from point sources in a turbulent channel flow, Aerosol Sci. Technol. 16 (4) (1992) 209–226.
[61] L. Talbot, R. Cheng, R. Schefer, D. Willis, Thermophoresis of particles in a heated boundary layer, J. Fluid Mech. 101 (4) (1980) 737–758.
[62] P. Saffman, The lift on a small sphere in a slow shear flow, J. Fluid Mech. 22 (2) (1965) 385–400.
[63] S.K. Das, S.U. Choi, W. Yu, T. Pradeep, Nanofluids: Science and Technology, John Wiley & Sons, 2007.
[64] W. Ranz, Evaporation from drops, Parts I & II, Chem Eng Prog. 48 (1952) 141–146.
[65] S. Tsorng, Three-dimensional particle paths in a lid-driven cavity flow: experiments and analysis (Ph.D. thesis), National Taiwan University, 2006.
[66] S. Tsorng, H. Capart, D. Lo, J. Lai, D. Young, Behaviour of macroscopic rigid spheres in lid-driven cavity flow, Int. J. Multiph. Flow. 34 (1) (2008) 76–101.
[67] S. Tsorng, H. Capart, J. Lai, D. Young, Three-dimensional tracking of the long time trajectories of suspended particles in a lid-driven cavity flow, Exp. Fluids 40 (2) (2006) 314–328.
[68] P. Kosinski, A. Kosinska, A.C. Hoffmann, Simulation of solid particles behaviour in a driven cavity flow, Powder Technol. 191 (3) (2009) 327–339.
[69] A.C. Baytaş, Entropy generation for thermal nonequilibrium natural convection with a non-Darcy flow model in a porous enclosure filled with a heat-generating solid phase, J. Porous Med. 10 (3) (2007).
[70] A. Bejan, Entropy Generation Minimization: The Method of Thermodynamic Optimization of Finite-Size Systems and Finite-Time Processes, CRC Press, 2013.
[71] S. Patankar, Numerical Heat Transfer and Fluid Flow: CRC Press, Taylor & Francis Group, LLC. Florida, United States, 1980.
[72] W.E. Boyce, R.C. DiPrima, D.B. Meade, Elementary Differential Equations and Boundary Value Problems, John Wiley & Sons, 2021.
[73] B. Yousefi-Lafouraki, A. Ramiar, A.A. Ranjbar, Modeling of two-phase particulate flows in a confined jet with a focus on two-way coupling, Particuology 39 (2018) 78–87.